The study of rs-fMRI ReHo features for patients with chronic fatigue syndrome among medical school students

Tie gang Wang[1,2], Zhong Ren Sun[2], Jun Wang[1], Xiang Xin Zeng[3], Jin Dai[3], Feng Wang[4], Danna Cao[4], Chuwen Feng[4], Weibo Sun[5], Yuanyuan Qu[2], Binbin Li[2], Liying Kathy Diao[67], Tiansong Yang[2]

1 Daqing Traditional Chinese Medicine Hospital, Daqing, China 2Heilongjiang University of Chinese Medicine, Harbin, China

3Second Affiliated Hospital, Harbin, China 4 First affiliated hospital, Heilongjiang University of Chinese Medicine, Harbin, China

5 The First Hospital of Harbing medical school, Harbin, China 6 Liying Acupuncture Healing Services, LLC, Columbia MD USA

7 John Hopkins Bloomberg School of Public Health, Baltimore MD USA

Background

Chronic fatigue syndrome (CFS) is a long-term and complex chronic disease that can lead to functional decline in patients. The main symptoms of the disease include unrelieved fatigue, cognitive impairment, and sleep disturbance. The quality of life of patients will be significantly reduced due to the above symptoms of CFS, and they will remain in this state for a long time, which will bring great cost and pressure to patients and the society, and it is not conducive to the recovery of patients. The epidemiological investigations on the incidence of CFS are not consistent at home and abroad. The consensus is that affected by environmental and psychological factors, the prevalence of CFS in women is 1.5-2 times that of men, and special populations (medical workers, soldiers, etc.) etc.) are approximately twice as common as the general population. Therefore, in recent years, neuroimaging methods, especially functional Magnetic Resonance Imaging (fMRI), which utilizes blood oxygen level dependent (BOLD) effects, have been widely used in the study of central pathological evolution of CFS. Regional homogeneity (ReHo) is a common analysis method in resting-state functional Magnetic Resonance Imaging (rs-fMRI) research, which reflects the activity level of local neurons in the human brain in the resting state.

Objective

To collect brain function data by rs-fMRI technology and use ReHo method to explore the differences in brain function between medical students with CFS and healthy control, and its correlation with clinical symptoms.

Methods

In the study, randomized, crossover design was used. 20 healthy subjects and 20 patients with CFS are recruited from medical school students. All subjects are evaluated by the scale corresponding to clinical symptoms and examined by fMRI scanning. Different activation states of brain function were compared between healthy subjects and patients with CFS. Different brain regions were found. Correlation analysis is conducted between ReHo values of different brain regions and clinical symptom scale scores.

Results

Compared with the normal group, in the CFS group, ReHo increased in the right thalamus and paracingulate gyrus, and decreased in the bilateral middle temporal gyrus. In the CFS group, the value of ReHo increased in the brain region was correlated with the score of the clinical symptom scale. There was a positive correlation between the right thalamus and the FS-14 score (r=0.7128, P=0.0004), a positive correlation with the SCL-90 score (r=0.4303, P=0.0498), a positive correlation with the PSQI score (r=0.4924, P=0.0274), and a negative correlation between the right paracingulate gyrus and the MoCa score (r=-0.4510, P=0.0460), However, the decreased brain area of ReHo had no significant correlation with the clinical scale score.

Conclusions

ReHo analysis found that, compared with the healthy control group, CFS patients had abnormal activation in the limbic system, basal ganglia, and other areas. There are significant differences in brain function ReHo in CFS patients. The involved brain areas are related to emotional, sensory, arousal and memory tasks, and are significantly related to clinical symptoms.

Keywords: medical school students; chronic fatigue syndrome (CFS); resting-state functional magnetic resonance imaging (rs-fMRI); regional homogeneity (ReHo)

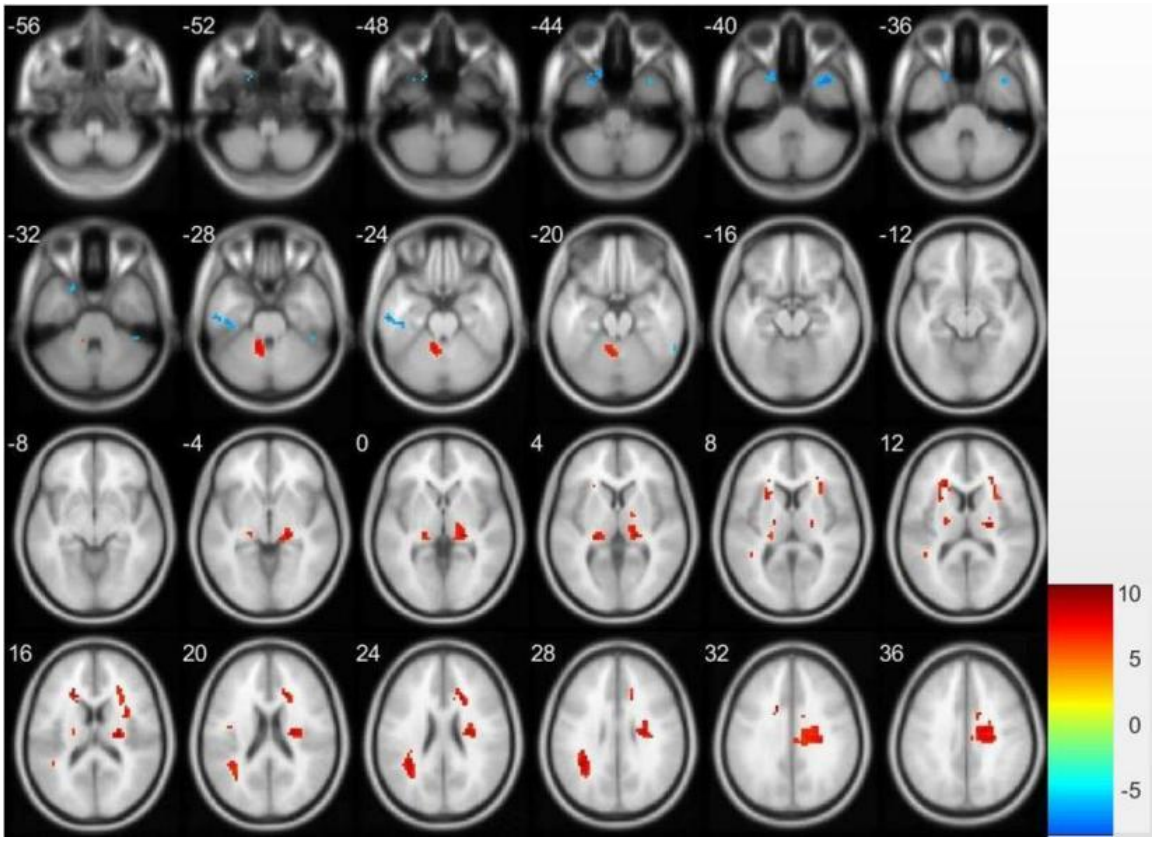

Figure 1 Cerebral areas exhibiting changes in ReHo values. Compare CFS case group vs. Control group.

Non-contrast assessment of blood-brain barrier permeability with arterial spin labeling (ASL) MRI

Zhiliang Wei, PhD[1,2], Hongshuai Liu, PhD[3], Zixuan Lin, PhD[1], Minmin Yao, PhD[3], Ruoxuan Li, MS[3], Chang Liu, MS[3], Yuguo Li, PhD[1,2], Jiadi Xu, PhD[1,2], Wenzhen Duan, PhD[3], Hanzhang Lu, PhD[1,2,4]

[1] Department of Radiology, Johns Hopkins School of Medicine, Baltimore, MD. [2] F. M. Kirby Research Center, Kennedy Krieger Research Institute, Baltimore, MD. [3]Department of Psychiatry and Behavioral Sciences, Johns Hopkins School of medicine, Baltimore, MD. [4] Department of Biomedical Engineering, Johns Hopkins School of Medicine, Baltimore, MD.

Background: Blood-brain barrier (BBB) permeability is a sensitive marker for various neurological disorders. Conventional techniques utilizing the extravasation principle of chemical agents (e.g., Evans Blue) share a common need of euthanization and thus are improper for longitudinal study.

Objective: We aimed to develop a non-contrast MRI technique for evaluating *in-vivo* BBB function in mice.

Methods: BBB permeability is evaluated with the principle that majority of water spins in the blood will be extracted by tissue and travel across the BBB, while the remaining will be drained to vein directly. Therefore, water extraction fraction (E) can be assessed by applying arterial spin labeling (ASL) MRI[1,2] at the venous side and, thereafter, permeability-by-surface-area product (PS) can be estimated with the Renkin-Crone equation.[3,4] We designed a series of experiments:[2] (1) post-labeling delay (PLD) optimization (N=5); (2) labeling duration (LD) optimization (N=5); (3) evaluating test-retest reproducibility (N=5); (4) applications to mouse model of Huntington's disease (HD; i.e., zQ175) (N=8 for wildtype; N=9 for HD); (5) histology validation of BBB leakage in HD model (N=5 for wildtype; N=4 for HD).

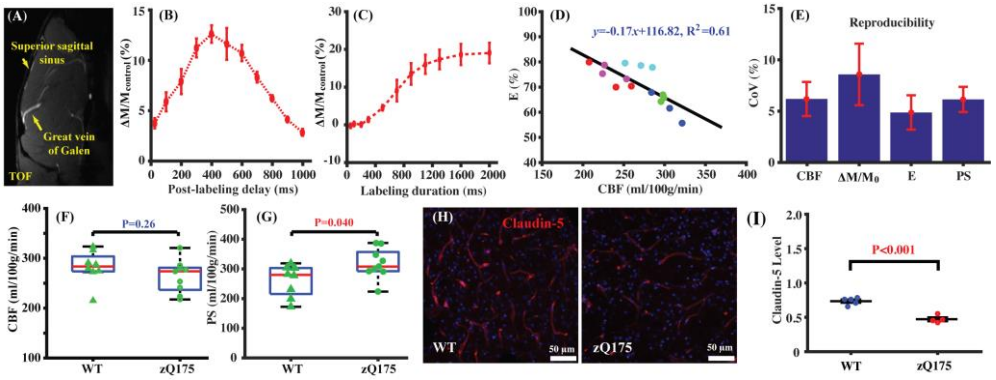

Figure 1 Non-contrast *in-vivo* assessment of BBB function. (A) time-of-flight (TOF) of midsagittal plane; (B and C) optimizations of PLD and LD; (D) correlation between CBF and water extraction (E: %); (E) coefficient-of-variation (CoV) for CBF, ASL signal, E, and PS; (F and G) CBF and PS in the zQ175 model; (H) immunofluorescent images of zQ175 model (Claudin-5: Red; DAPI: blue); (I) Claudin-5 content in zQ175 model by Western blot analysis.

Results: In mice, great vein of Galen is much larger than superior sagittal sinus (Fig. 1A), and therefore is focused for better sensitivity. Bolus arrival time to vein (BAT_{vein}) is 691.2±14.5 ms (Fig. 1B; N=5) and full-width-of-half-maximum (FWHM) of dispersion is 806.4±65.4 ms (Fig. 1C; N=5). Based on these physiological measurements, an LD=1200 ms with PLD=100 ms is a decent trade-off among sensitivity, scan duration, and specific absorption rate (SAR). In the test-retest reproducibility study, we found a negative correlation between E and basal CBF ($P<0.001$; Fig. 1D), consistent with the fact that, under higher CBF, water spins stay at the capillary bed for a shorter time and allow less opportunity for extraction. Averaged CoV values were 6.2±1.7%, 8.6±3.0%, 4.9±1.7%, and 6.1±1.2% for CBF, $\Delta M/M_0$, E, and PS, respectively (Fig. 1E; N=5), suggesting satisfactory reproducibility for these physiological measurements. In the zQ175 model, HD mice were associated with similar perfusion (Fig. 1F) but higher PS (i.e., leakier BBB) (Fig. 1G). Immunofluorescent staining revealed reduced Claudin-5 (a kind of tight-junction proteins [TJPs]) density in the zQ175 (Fig. 1H). Alterations in the three major TJPs (i.e., ZO-1, Occludin, and Claudin-5) were further verified with the Western blot analyses. There were significant alterations in Claudin 5 ($P<0.001$; Fig. 1I), ZO-1 ($P<0.05$), and Occludin ($P<0.05$) (data now shown for page limit).

Conclusions: We developed a quantitative MRI method for *in-vivo* measurement of BBB function in mice. The optimized MRI protocol exhibits decent test-retest reproducibility. Application to the mouse model of Huntington's disease supports the feasibility and effectiveness of our method in studying the dynamic BBB status in the neurodegenerative diseases.

References: 1. Hirschler L *et al.* Magn Reson Med (2018) 79:1314. 2. Wei Z *et al.* NeuroImage (2023) 268:119870. 3. Renkin E. Am J Physiol (1959) 197:1205. 4. Crone C. Acta Physiol Scand (1963) 58:292.

Bridging Vascular and Neurological Domains: Insight into Cerebral Metabolic Changes due to Arterial Calcification

Eric M. Teichner BA[1], Robert C. Subtirelu MSc[2], Poul Flemming Høilund-Carlsen MD PhD[3], Mona-Elisabeth Revheim MD PhD[4], Thomas J. Werner MSE[2], Abass Alavi MD[2]

[1]Sidney Kimmel Medical College, Thomas Jefferson University, Philadelphia, PA.
[2]Department of Radiology, Hospital of the University of Pennsylvania, Philadelphia, PA.
[3]Department of Nuclear Medicine, Odense University Hospital, 5000 Odense C, Denmark
[4]Institute of Clinical Medicine, University of Oslo, Oslo, Norway.

Introduction: Cardiovascular disease (CVD) is a broad categorization of various diseases that affect the heart and arterial blood vessels. It is important to quantify the extent of molecular calcification within the carotid arteries because patients with, or at risk of developing CVD have an increased incidence of cognitive impairment. Metabolic abnormalities, which can be directly measured by 18F-fluorodeoxyglucose positron emission tomography (FDG-PET), correlate with worse performance on both cognitive tests and activities of daily living measures. 18F-sodium fluoride (NaF)-PET, a valid method of assessing molecular calcification and therefore atherosclerosis, can be utilized to detect and quantify this disease in patients with CVD or multiple cardiovascular risk factors (CRFs) and controls. The reported literature has not clearly correlated actual arterial disease throughout the body with cerebral hypometabolism.

Objective: In this study, we correlated the degree of molecular calcification within the left common carotid (LCC) artery with regional cerebral fluorodeoxyglucose (FDG) uptake in patients with CRFs.

Methods: In total, 36 subjects (mean age 55.4 ± 12.3 years, 50% males) with known CRFs underwent FDG-PET scanning, and 70 whole brain structures were analyzed in each subject. Participants were recruited from a group of patients with chest pain syndromes who were referred for coronary CT angiography. All subjects underwent whole-body FDG-PET/CT imaging 180 minutes after the administration of 4.0 MBq/kg dose of FDG. NaF-PET/CT was performed 90 min after the intravenous injection of 2.2 MBq of NaF per kilogram of body weight. NaF uptake in the LCC was quantitatively assessed by measuring the blood-pool-corrected maximum standardized uptake value (SUVmean) on each axial slice. The quantitative regional analysis of PET images was performed using MIMneuro version 7.1.5 (MIM Software, Inc., Cleveland, Ohio). MIMneuro provided cerebral region-based analysis, with z-scores generated by comparing the patient to the selected age-matched set of normal controls. Pearson's R was calculated and evaluated for significance in all variables. The threshold for significance was set at $P < 0.05$.

Results: Various significant associations between NaF uptake in the LCC artery and FDG uptake across all 70 brain regions of interest were observed. In particular, NaF uptake was found to have an inverse correlation with regional metabolism in the anterior cingulate gyrus ($r = -0.344$, $p=0.040$), cingulate gyrus ($r=-0.358$, $p=0.032$), inferior frontal gyrus ($r=-0.336$, $p=0.045$), and the inferior frontal gyrus pars opercularis ($r=-0.346$, $p=0.039$)

Conclusions: LCC calcification, as measured by NaF uptake, was found to have an inverse relationship with metabolic activity in four specific brain regions, as measured by FDG uptake. Previous research has reported that reduced perfusion in the cingulate gyrus, which is thought to be involved in declarative and procedural memory, may explain why hypoxia causes working memory problems. Furthermore, reduced relative blood flow, as measured by single photon emission computed tomography (SPECT), within the posterior cingulate gyrus is found years before patients meet the clinical diagnostic criteria of Alzheimer's disease. In addition, studies have shown that the inferior frontal gyrus is associated with executive deficits in early dementia. Through the demonstrated correlations, our results provide insight into the pathoanatomical mechanisms responsible for memory deficits observed in various dementias. NaF-PET and FDG-PET can provide valuable insights into the underlying biological processes of cardiovascular and neuronal degeneration.

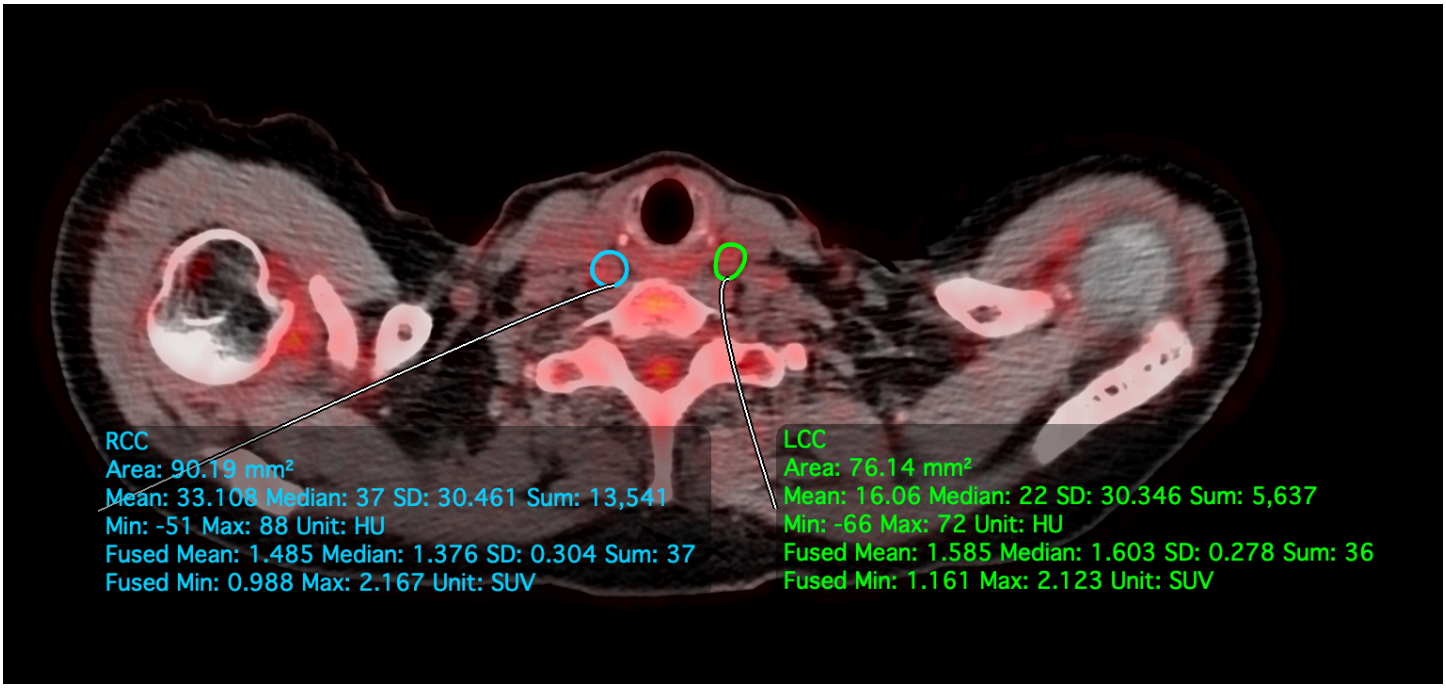

Figure 1. Quantitative assessment conducted by defining regions of interest (ROI) around the left (LCC) and right (RCC) common carotid arteries. LCC was the primary measure of carotid atherosclerosis in this study. For the drawn LCC ROI, SUVmean = 1.585, SUVmin = 1.161 and SUVmax = 2.123.

Utility of Total Lesional Glycolysis in Characterizing Liver Metastases in Patients Undergoing Ablation

Fereshteh Yazdanpanah[1], Omar Al Daoud[1], Mamduh Alatout[1], Moein Moradpour[1], Raisa Amiruddin[1], Thomas Werner[1], Abass Alavi[1], Stephen J. Hunt[1]

[1] Department of Radiology, Hospital of University of Pennsylvania (HUP), Universith of Pennsylvania, Philadelphia 19104, PA, USA

Background: Total lesion glycolysis (TLG) is a quantitative FDG PET-CT measure incorporating both metabolic activity and volume assessment of tumor burden.

Objective: This study examines the utility of TLG as a quantitative marker of disease burden and treatment response in the setting of percutaneous ablation of liver metastases.

Methods and Materials: An IRB-approved retrospective analysis of patients undergoing liver ablation for metastatic disease at a single academic medical center from January 2014 to January 2022 identified from an IR quality database (Hi-IQ), and having both pre and post ablation PET-CT within one year of ablation. TLG in the ablated tumor was determined using an automated adaptive contrast-oriented thresholding method (ROVER, ABX GmbH). Two-tailed paired t-tests were conducted to compare FDG-PET/CT scan parameters before and after ablation. Kaplan-Meir analysis was used to compare outcome data.

Results: 447 patients underwent liver mass ablation during the study interval. Among these patients, FDG-PET imaging was performed in 59 patients, and 20 patients had both baseline and follow-up PET-CT (12 M; 8 F). Median age was 61 (54.2-72) with a median follow-up of 22.5 months (14.2-54.7). Five patients underwent multiple ablations. Origin of metastases included colorectal cancer (10), lung cancer (7), tonsilar squamous cell carcinoma (1), cholangiocarcinoma (1) and pancreatic adenocarcinoma (1). 17 patients experienced intrahepatic recurrence during follow-up with a mean interval of 6 months (range: 1-27 months). Pre-ablation and post-ablation TLG of the lesions were significantly different ($p < 0.01$). 18 out of 20 patients demonstrated decrease in TLG consistent with response to ablation, while two patients demonstrated increase in tumor TLG, consistent with ablation mistargeting (Figure 1). Complete response to ablation was defined as post-ablation TLG<2, with 11 patients meeting criteria for complete ablation with a mean TLG of 0.2 (range 0.1-1.6). Complete responders had a decrease of 98% or greater between pre and post TLG. The remaining 10 patients had post-ablation TLG of >2, with a mean post-ablation TLG of 30 and TLG decrease of 59% (range 25-83%). Post-ablation survival (mean+/-sem) differed significantly between complete ablation responders (37+/-7 months) and incomplete responders (27+/-7 months; $p<0.1$).

Conclusion: Total lesion glycolysis provides a quantitative assessment of disease burden and response to liver metastasis ablation, and post-ablation TLG of >2 is associated with poorer survival outcomes.

Clinical Relevance: TLG provides a quantitative assessment of tumor burden and response to ablation.

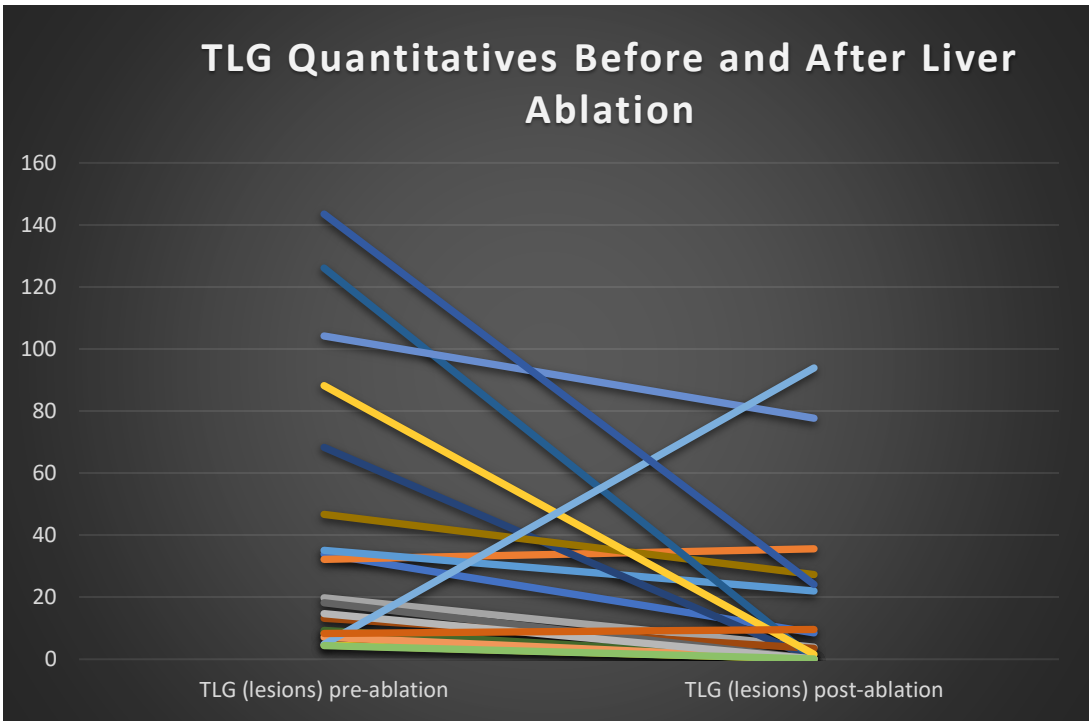

Determining magnetic nanoparticle blood half-life and tumor retention using MPI: Relevance to targeted, image-guided magnetic hyperthermia

Marzieh Salimi Ph.D., Shreyas Kuddannaya Ph.D., Jeff W.M. Bulte Ph.D.

Department of Radiology and Radiological Science, Johns Hopkins University, Baltimore, MD, USA

Background: MPI is a non-invasive tomographic modality that directly detects magnetic nanoparticles (MNPs). Recently, MPI-guided magnetic hyperthermia (MH) has been developed to achieve targeted tumor heating while sparing normal tissues[1], which will be critical for precision-based clinical translation[2]. In most MH studies, MNPs have been injected intratumorally. However, ideally, they are injected systemically to also reach (occult) metastases through specific targeting or non-specific enhanced permeability retention. For systemic i.v. injection, the blood clearance of MNPs is a critical pharmacologic parameter.

Objective: We present here a novel MPI blood assay that can be used to precisely calculate MNP blood half-life without the need of modifying them with other (radioactive) labels that may alter their biodistribution. In addition, we show how MPI can be used to quantify intratumorally injected MNPs as relevant for future MPI-guided MH.

Methods: Systemic injection: Female rats weighing 200 g underwent femoral vein and femoral artery catheterization. Synomag-D70 and Synomag-D50 MNPs (MicroMod) were injected into the femoral vein at a dose of 2 mg Fe in 1.0 ml PBS (n=3). Using a pin port-injector, blood samples (300 µL) were drawn from the femoral artery at various time points after injection (baseline, 1, 5, 10, 15, 30, 60, and 120 min). After withdrawal at each time point, 300 µL of PBS was re-injected intra-arterially to compensate for loss of blood volume. The MPI signal of heparinized blood samples was measured with a pre-clinical Momentum MPI scanner using the RELAX module. The same samples were also measured for total Fe content using a spectrophotometric-based method (Ferrozine-assay) specific for iron. Intratumoral injection: Mice (BALB/c, n=3) bearing s.c. 4T1 breast cancer tumors were injected with Synomag-D70 and Synomag-D50 MNPs (50 mg/mL in 1/27 of tumor volume). 3D MPI (Momentum scanner) and micro-CT (SARRP scanner) images were obtained 5 min and 24 h after injection, respectively, and co-registered using MagImage software. To quantify the MNP signal and MNP tumor retention, calibration 3D MPI scans were obtained for 20 µL MNP samples containing (0, 0.1, 0.5, 1, 5, 10, and 50 mg Fe/mL). **Results:** The blood half-lives of Synomag-D70 and Synomag-D50 MNPs were calculated using both mono- and bi-exponential curve fittings. Synomag-D 70 exhibited a biexponential clearance with a half-life of 2.72±0.53 min (79.13% weighting, R=0.99)(**Fig. 1A**), while Synomag-D 50 exhibited a monoexponential clearance with a half-life of 11.44±4.26 min (56.37% weighting, R=0.99)(**Fig. 1B**). The spectrophotometric Ferrozine-assay was not accurate due to the high background iron content from haemoglobin (red blood cells). Co-registered MPI-CT images of Synomag-D70 and Synomag-D50 MNPs injected intratumorally are shown in **Fig. 1C**. MPI quantification revealed that 42.3±17.8% and 40.0±16.6% of Synomag-D70 and Synomag-D50, respectively, were retained in the tumor 5 min after injection (**Fig. 1D**).

Conclusions: Conventional methods for measuring the pharmacokinetic biodistribution profiles of MNPs rely on radiolabelling them, but have significant drawbacks including instability and leaching of radioactive tracers, altered biodistribution, as well as logistics for radiation hazards. Previously, the blood half-life of native, unlabelled MNPs could only be quantified by measuring T2 NMR relaxation times[3,4]. While a simple Ferrozine assay was unable to yield reliable data, we demonstrated that MPI is a straightforward, simple, specific, and sensitive method capable of detecting even small amounts of MNPs without interference from endogenous blood iron. In addition, MPI appears to be also a robust tool for quantifying the amount of injected and retained MNPs within tumors, paving the way for future studies using MPI-guided MH.

References: 1. Tay ZW et al., ACS Nano 24, 3699-3713 (2018). 2. Healy S et al., Wiley Interdiscip. Rev. Nanomed. Nanobiotechnol. 14, e1779 (2022). 3. Bulte JWM et al., Acad. Radiol. 2, 871-878 (1995). 4. Bulte JWM et al., JMRI 9, 329-335 (1999).

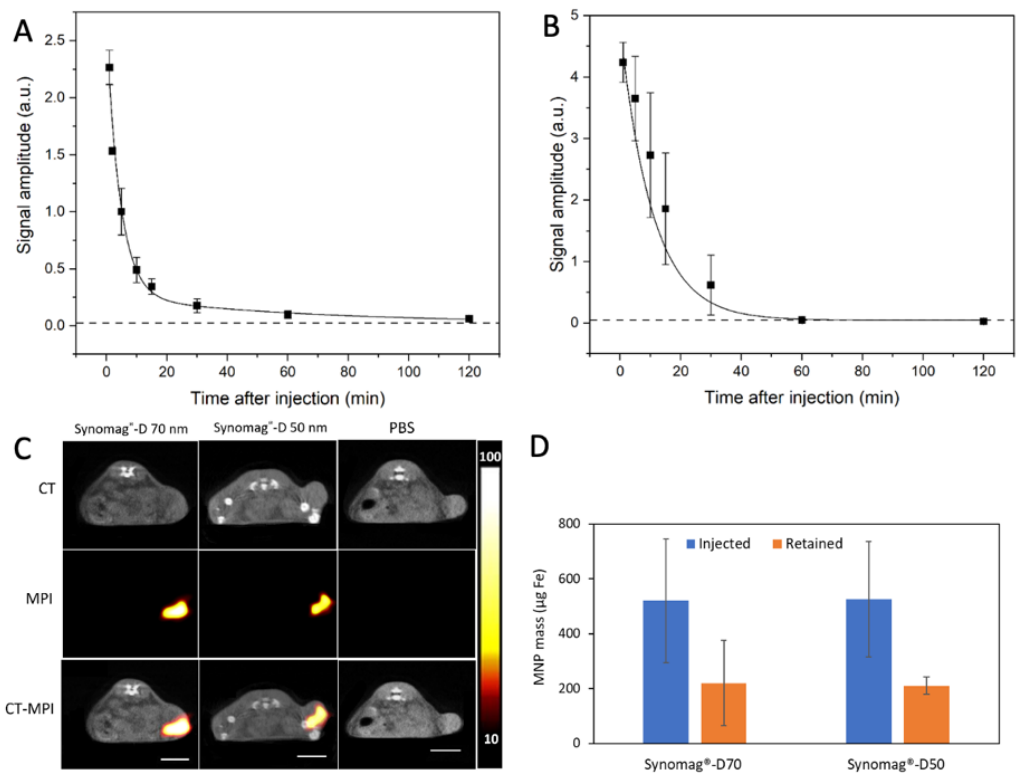

Figure 1. MPI blood clearance curves for i.v. injected (A) Synomag-D70 and (B) Synomag-D50. (C) MPI/CT co-registered images taken 5 min and 24 h, respectively, after intratumoral injection of Synomag-D70, Synomag-D50, and control (PBS). (D) MPI quantification of the retained amount of Synomag-D70 and Synomag-D50 5 min after intratumoral injection compared to the amount that was initially injected.

3D printing-based frugal manufacturing of glass pipettes for minimally invasive delivery of therapeutics to the brain

David Gulisashvili MD[1], Guanda Qiao MD, PhD[1], Anna Jablonska PhD[1], Guiling Zhao PhD[2], Miroslaw Janowski MD, PhD[1], Piotr Walczak MD, PhD[1], Yajie Liang MD, PhD[1]

[1]Department of Diagnostic Radiology and Nuclear Medicine, University of Maryland School of Medicine, Baltimore, Maryland, USA

[2]Laboratory of Molecular Cardiology, Department of Physiology, Center for Biomedical Engineering and Technology, University of Maryland School of Medicine, Baltimore, Maryland, USA

Background. Various routes are used to administer therapeutics to the brain, with intracerebral injection offering precise targeting and direct access to the brain tissue [1-8]. However, their invasiveness and tissue damage are their drawbacks. Glass pipettes, with thinner tips and smoother surfaces, are being increasingly used for delivering therapeutics to the brain. To address accessibility and affordability issues, an open-source 3D printable device was designed to pull glass pipettes, making them more accessible to laboratories and facilitating preclinical studies.

Objective. The intracerebral delivery of agents in liquid form is usually achieved using commercially available and durable metal needles. However, their size and texture may contribute to mechanical brain damage. Glass pipettes with a thin tip may significantly reduce injection-associated brain damage, but require access to prohibitively expensive programmable pipette pullers. This study aimed to eliminate the economic barrier to the application of minimally invasive delivery of therapeutics to the brain, such as chemical compounds, viral vectors, and cells.

Methods. We took advantage of the rapid development of free educational online resources and the emergence of low-cost 3D printers by designing an affordable pipette puller (APP) to eliminate cost obstacles.

Results. The affordable pipette puller (APP) (Fig.1 A-E) achieved a high success rate in producing glass pipettes with thin tips suitable for brain drug delivery. To test the durability of a single APP, we continuously pulled 25 times with a 100% success rate of production. The glass pipettes generated using APP had a diameter of <20μm, making them thin enough for the precise delivery of therapeutics to the brain. The comparison between the APP and a programmable pipette puller revealed that the necks of the glass pipettes were longer with the APP due to the delay time after heating, based on pulling force ranging from 1.0 N to 26.0 N, and their tips had a diameter of a few micrometers (Fig.1 F). The APP nanoliter-scale injector system enabled high-precision fluid delivery at 0.2nL/μm progression, and its 30μm OD glass pipettes demonstrated less brain damage with a narrower track compared to a 33-gauge Hamilton syringe needle (210μm diameter) when injecting fluorescent beads into the mouse brain (Fig.1 G).

Conclusions. In the spirit of frugal science, our device may democratize glass pipette-puling and substantially promote the application of minimally invasive and precisely controlled delivery of therapeutics to the brain to find more effective therapies for brain diseases.

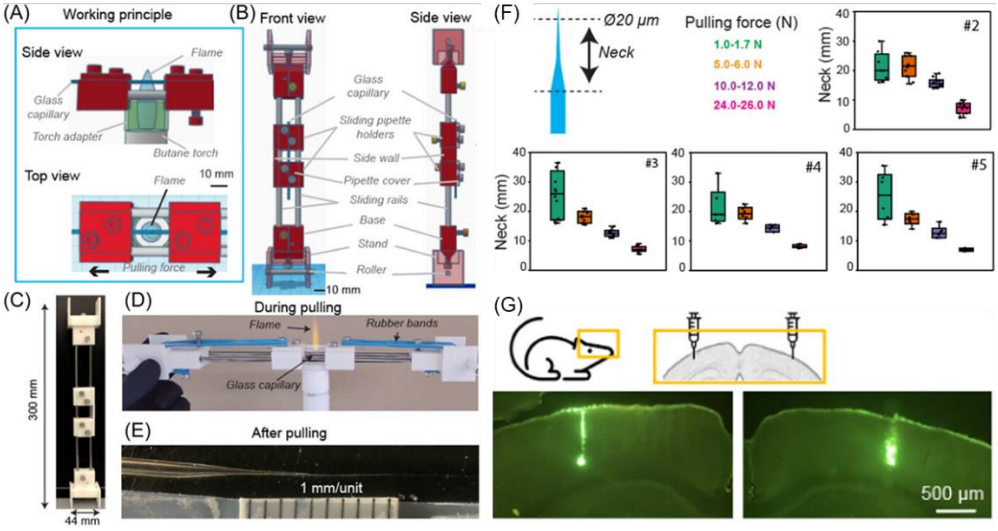

Figure. 1. Design of the affordable pipette puller (APP). **(A)** Working principle of APP. Side and top view of the APP in action. **(B)** The design and components from our APP. **(C)** Assembled APP with the dimension of 300 (height) × 44 (width) × 30 (length). **(D)** Pulling procedure. **(E)** After pulling, a thin pipette tip is formed with a long neck. **(F)** The definition of the length of the neck and neck distance under different pulling forces (1.0–1.7 N, 5.0–6.0 N, 10.0–12.0 N, 24.0–26.0 N) and flame heights (#2 through #5). The definition of the length of the neck and neck distance under different pulling forces (1.0–1.7 N, 5.0–6.0 N, 10.0–12.0 N, 24.0–26.0 N) and flame heights (#2 through #5). **(G)** Injection of fluids into the mouse brain through glass pipettes (left) or a Hamilton syringe needle (right) with representative histology images showing the needle tracks, respectively.

1. Misra V, Ritchie MM, Stone LL, Low WC, Janardhan V. Stem cell therapy in ischemic stroke: role of IV and intra-arterial therapy. Neurology. 2012; 79(13 suppl 1): S207- S212.
2. Pardridge WM. Drug and gene delivery to the brain. Neuron. 2002; 36(4): 555- 558.
3. Modo M, Stroemer RP, Tang E, Patel S, Hodges H. Effects of implantation site of stem cell grafts on behavioral recovery from stroke damage. Stroke. 2002; 33(9): 2270- 2278.
4. Jiang Q, Zhang ZG, Ding GL, et al. Investigation of neural progenitor cell induced angiogenesis after embolic stroke in rat using MRI. Neuroimage. 2005; 28(3): 698- 707.
5. Dong X. Current strategies for brain drug delivery. Theranostics. 2018; 8(6): 1481- 1493.
6. Kawabori M, Shichinohe H, Kuroda S, Houkin K. Clinical trials of stem cell therapy for cerebral ischemic stroke. Int J Mol Sci. 2020; 21(19):7380.
7. Savitz SI, Dinsmore J, Wu J, Henderson GV, Stieg P, Caplan LR. Neurotransplantation of fetal porcine cells in patients with basal ganglia infarcts: a preliminary safety and feasibility study. Cerebrovasc Dis. 2005; 20(2): 101- 107.
8. Kondziolka D, Steinberg GK, Wechsler L, et al. Neurotransplantation for patients with subcortical motor stroke: a phase 2 randomized trial. J Neurosurg. 2005; 103(1): 38- 45.

In Vivo Tracking of Genome-Edited iPSC-Derived NPCs in ALS Mice Using MPI/BLI

A. Shakeri-Zadeh[1,2], Ph.D., S. Kuddannaya[1], Ph.D., C. Zivko[2,3], Ph.D., V. Mahairaki[2,3], Ph.D., J. Bulte[1,2], Ph.D.

[1]The Russell H. Morgan Department of Radiology and Radiological Science, Division of MR Research, Baltimore, MD, USA; [2]Cellular Imaging Section and Vascular Biology Program, Institute for Cell Engineering, Baltimore, MD, USA; [3]Department of Genetic Medicine, Johns Hopkins University School of Medicine, Baltimore, MD, USA; [4]The Richman Family Precision Medicine Center of Excellence in Alzheimer's Disease, Johns Hopkins University School of Medicine, Baltimore, MD, USA.

Background: Approximately 20% of amyotrophic lateral sclerosis (ALS) cases are caused by a mutation in the gene superoxide dismutase 1 (SOD1), leading to familial ALS. Induced pluripotent stem cell (iPSC)-based therapies, aimed at restoring normal motor neurons in ALS patients, hold promise as a therapeutic approach, contingent upon the use of genetically corrected patient-derived cells. To pursue mutant SOD1-edited iPSC therapy effectively, it is crucial to have non-invasive imaging techniques available that can provide longitudinal data on the fate of transplanted cells. Magnetic particle imaging (MPI) enables the visualization and quantification of superparamagnetic iron oxide (SPIO)-labeled stem cells in a specific manner. Bioluminescence imaging (BLI) is another method for cell tracking that enables us to monitor the viability of transplanted cells over time.

Objective: To track and quantify neural precursor cells (NPCs) derived from mutant SOD1-edited iPSCs using MPI/BLI *in vivo*.

Methods: The human 39B2.5 iPSC cell line, genetically edited for the mutant SOD1 gene, was first differentiated into NPCs. NPCs were engineered to express luciferase through the introduction of the Nanoluc gene. Luciferase activity in NPCs was studied *in vitro* using the fluorofumarizine (FFz) substrate. Nanoluc-NPCs were labeled with SPIO (Resovist®, 28 µg Fe/ml, 2 h) and then transplanted into immunosuppressed transgenic SOD1^{G93A} mice. 200,000 labeled Nanoluc-NPCs were stereotaxically injected into either the motor cortex (MC) or ventral horns of the C3-C4 spinal cord (SC). Serial *in vivo* BLI was performed to monitor the luciferase signal intensity/photon flux (photons per second) using Living Image software. 2D/3D standard MPI and CT were conducted using Magnetic Insight Momentum and Perkin Elmer IVIS Spectrum/CT scanners, respectively. For MPI data co-registration, two fiducials with 60,000 and 30,000 cells in 20 ul of PBS were positioned next to the mice in the same field of view. To determine the iron content of the fiducials and calculate the amount of iron per cell, a linear regression analysis was conducted using reference samples of Resovist.

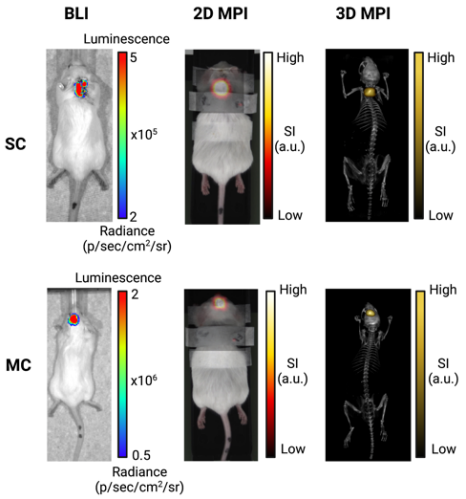

Figure 1. Representative *in vivo* BLI and 2D/3D MPI scans of ALS mice 30 min after receiving SPIO-labeled Nanoluc-NPCs. BLI shows luciferase signal intensity, while MPI/CT provides high-resolution imaging of the distribution and localization of transplanted cells in the brain and SC.

Results: We successfully generated gene-edited iPSC-derived NPCs and confirmed luciferase expression within these cells through *in vitro* validation with the FFZ substrate. SPIO-labeling of Nanoluc-NPCs was also accomplished successfully. Upon transplantation of these labeled NPCs into the brains and spinal cords of ALS mice, we were able to track their distribution and viability *in vivo* using BLI and MPI (**Fig. 1**). The accuracy of successful transplantation in both MC and SC is evident. Through regression analysis, we determined that the iron content of transplanted cells was approximately 10 pg per cell. By correlating the MPI signal intensity of the brain or spinal cord with fiducial information, we estimated cell numbers of 239,000 and 237,000 for the SC MC injections, respectively. Discrepancies between the theoretical and experimental cell numbers may arise from errors during pipetting, cell counting, loading cell suspensions into syringes, injection, and the presence of blooming artifacts.

Conclusions: Our results demonstrate successful tracking and quantification of SPIO-labeled Nanoluc-NPCs in an ALS mouse model. These findings may contribute to advance non-invasive cell tracking methodologies for treatment of neurodegenerative diseases.

^{18}F-NaF as a biomarker of osteoporosis and bone fragility in multiple myeloma: ^{18}F-NaF and ^{18}F-FDG PET/CT study

Peter Sang Uk Park[1], Lori Jia[1], William Y Raynor[1], Mia Mijung Park[1], Om H. Gandhi[1], Thomas J Werner[1], Poul Flemming Høilund-Carlsen[2,3], Abass Alavi[1]

Department of Radiology, Hospital of the University of Pennsylvania, Philadelphia, PA, United States[1],
Department of Nuclear Medicine, Odense University Hospital, Odense, Denmark[2],
Department of Clinical Research, University of Southern Denmark, Odense, Denmark[3]

Background:
Multiple myeloma is a neoplasm of B plasma cells in the bone marrow primarily affecting the bone by inducing osteoporosis, osteolytic lesions, and fractures with devastating consequences. Detecting molecular changes in bone metabolism, such as reduced osteoblastic activity and bone remodeling associated with multiple myeloma, would allow for early diagnosis of osteoporosis in the lumbar spine and reduce risk for surgical spinal interventions. 18F-sodium fluoride (NaF)-PET/CT is such an imaging modality with potential for early and late detection of wide arrange of bone pathologies including osteoporosis, active bone lesions, and fractures. 18F-fluorodeoxyglucose (FDG) on the other hand is an established radioactive tracer for the detection of extraosseous involvement of multiple myeloma.

Objective:
To assess the capability of 18F-NaF and 18F-FDG PET/CT for evaluating osteoporosis and fractures in the lumbar spines of patients with multiple myeloma.

Methods:
We measure the standardized uptake values (SUV) of tracers 18F-NaF and 18F-FDG in the L1-L4 spines of newly diagnosed 33 multiple myeloma patients (24 men, 9 women; mean age 66.6 ± 8.6 years) from the FULIMA trial (NCT02187731). We used the OsiriX software version 12.0 (Pixmeo, Bernex, Switzerland) to define regions of interest (ROIs) drawn at the trabecular bone from the CT images that were then co-registered with PET scans to derive standardized uptake values (SUV). The SUV values are evaluated for correlation with age and mean Hounsfield unit (HU) and tested for the ability to distinguish between those with osteoporosis or fractures versus without. To test the diagnostic ability of SUV uptake values for osteoporosis or fractures, receiver-operating characteristic (ROC) curves were generated, and Wilson/Brown method was used to calculate the area under the curve (AUC).

Results:
Out of the 33 subjects, twelve were deemed to have osteoporosis (9 men, 3 women) with mean HU of 79.4 ± 15.8, while eleven had a presence of fracture, most common being a vertebral compression fracture. Out of all the SUV values, 18F-NaF SUVmin had the strongest correlation with both mean HU and age (mean HU: $p < 0.0001$; age: $p = 0.0008$) followed by 18F-NaF SUVmean (mean HU: $p < 0.000$; age: $p = 0.002$), and 18F-NaF SUVmax (mean HU: $p = 0.01$; age: $p = 0.04$). None of the 18F-FDG values were correlative. All three 18F-NaF SUV values were predictive for osteoporosis (**Figure 1**). However, only 18F-NaF SUVmin was predictive of presence of fractures (AUC: 0.83, $p = 0.002$).

Conclusion:
Our study showed that ^{18}F-NaF uptake correlates with bone density as measured by HU and age at the L1-L4 spine. On the other hand, ^{18}F-FDG uptake did not show any correlation. In terms of predicting the presence of osteoporosis or fractures, ^{18}F-NaF SUVmin demonstrated the best potential as the biomarker of molecular bone turnover. Future studies could further evaluate the role of ^{18}F-NaF SUVmin in prospective studies and consider ^{18}F-NaF-PET as a synergistic test to ^{18}F-FDG-PET/CT.

Keywords: 18F-NaF, 18F-FDG, PET, biomarker, osteoporosis, fractures, multiple myeloma

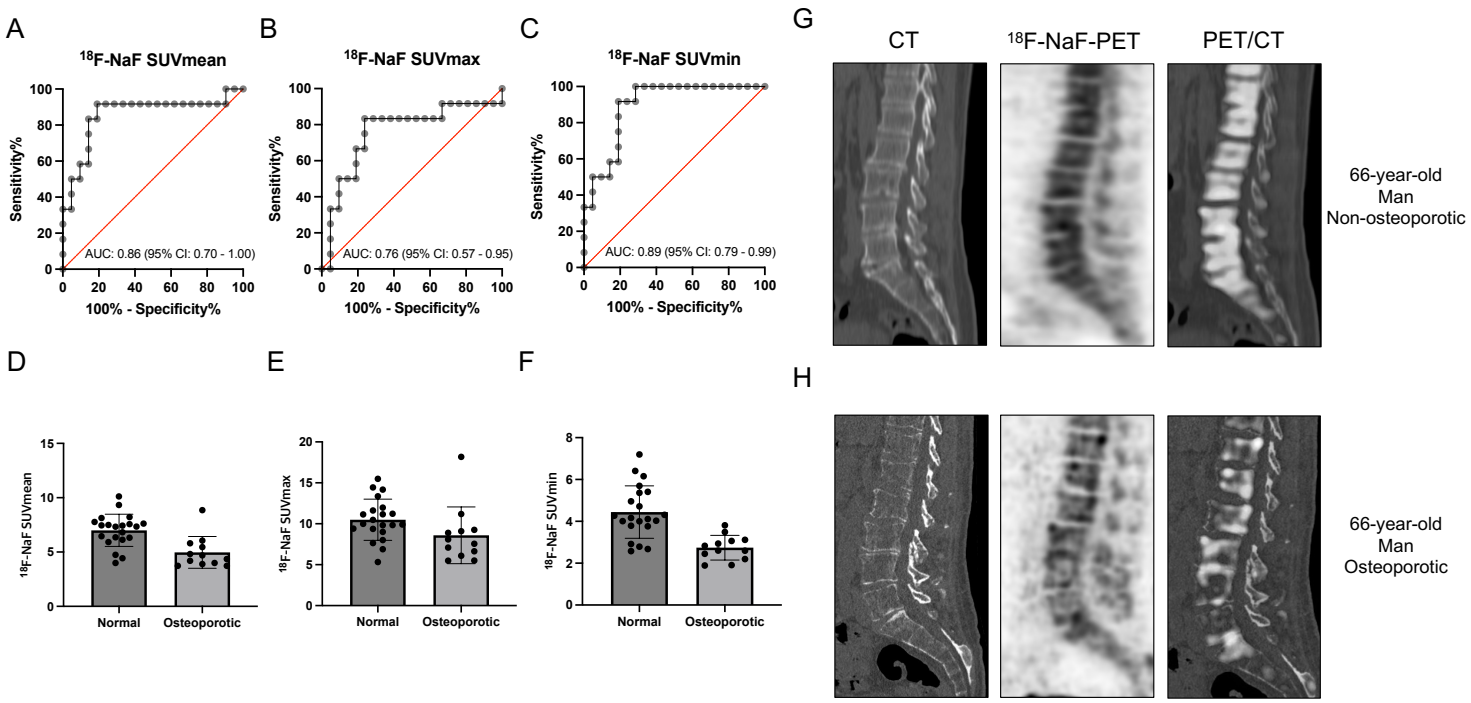

Figure 1. 18F-NaF PET for assessing for osteoporotic bone in patients with multiple myeloma. ROC curves demonstrating the performance of 18F-NaF-PET SUVmean (A), SUVmax (B) and SUVmin (C) in differentiating normal versus osteoporotic bone. Bar graphs showing the difference of 18F-NaF-PET SUVmean (D), SUVmax (E), and SUVmin (F) in normal versus osteoporotic bone. Representative CT, PET/CT, and PET images of age-matched patients with lumbar spines of normal mineral density (G) and osteoporotic quality (H).

Non-invasive spatial characterization of PD-L1 expression following Immune Checkpoint Therapies

Akhilesh Mishra, Kuldeep Gupta, Dhiraj Kumar, Sridhar Nimmagadda
Russell H. Morgan Department of Radiology and Radiological Sciences, Johns Hopkins University, Baltimore, MD, United States

Background: While immunotherapy utilizing immune checkpoint inhibitors (ICIs) has led to significant improvements in the survival of patients with certain cancers, efforts are underway to improve the response rates[1]. The majority of combination therapies upregulate programmed death-ligand 1 (PD-L1), which also correlates with the treatment response to several ICIs[2]. Emerging clinical and preclinical evidence indicates that the presence of PD-L1 towards the core of the tumors appears to function of infiltrated CD3+ T cells[3]. However, presence of intratumor heterogeneity observed with PD-L1 in clinical trials, poses a challenge when using PD-L1 expression from single tumor biopsies as a reliable predictor for immunotherapy response[4,5]. Thus, Positron Emission Tomography (PET) imaging could help reveal spatial distribution of PD-L1 expression, thus inform upon immune-cell infiltration and possibly predict response to different ICIs[6].

Objective: To investigate and compare the spatial distribution profile of PD-L1, using [^{18}F]DK222 PET (a peptide-based imaging agent), in tumors under monotherapy and combination therapy.

Methods: NSG mice humanized with CD34+ cells were engrafted with A375 melanoma xenografts. The mice were randomized: one received 5 mg/kg of anti-PD-1 (pembrolizumab), while the other received a combination of 5 mg/kg of anti-PD-1 and 4 mg/kg of anti-CTLA-4 (ipilimumab) (n=5). [^{18}F]DK222 PET imaging was conducted before treatment initiation and 7 days after treatment started. 3 mm distance from center was chosen to define core of the tumors. Standardized uptake values (SUV) were calculated by normalizing for net injected activity and mouse weight. Data transformed using RStudio's tidyverse package for compatibility with other packages. Plotly and plot3D from RStudio used for 2D and 3D plots. To validate the PET results, immunohistochemistry (IHC) was performed (#13684, Cell Signaling Technology at 1:500 dilution).

Results: We visualized intensity of [^{18}F]DK222 distribution across the tumor as a measure of PD-L1 expression. We observed that tumors of mice before treatment had small SUVs, of less than 2 indicating low PD-L1 levels **(Fig A**; left panels). Most of this signal was localized at the tumor periphery**.** Following immunotherapy, there was a significant increase in [^{18}F]DK222 SUV distributed in the core of the tumors indicating upregulation of PD-L1 **(Fig A**; right panels). Furthermore, [^{18}F]DK222 SUVs were higher for combination treatment than that for monotherapy, indicating differences in therapy induced PD-L1 levels by different treatments. At the periphery of the tumors, PD-L1 expression, as measured using [^{18}F]DK222 SUV, in pretreatment group was 0.84±0.28. PD-L1 expression following aPD-1 monotherapy significantly increased to 1.19±0.49 ($p<0.0001$) **(Fig B**; left). Combination therapy showed higher PD-L1 upregulation (SUV 2.38±0.75, $p<0.0001$). These differences were further amplified in the core, with combination treatment showing highest PD-L1 upregulation (SUV 4.34±0.65), followed by aPD-1 monotherapy (SUV 1.92±0.30, $p<0.0001$) **(Fig B**; right). These results showed that PD-L1 upregulation following immunotherapy is stronger towards the core of the tumor than the periphery. IHC analysis further corroborated these PET findings **(Fig C-D)**.

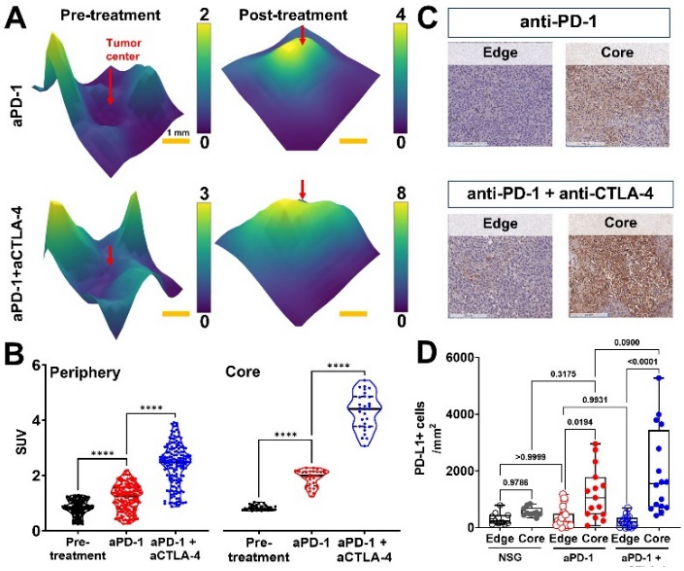

Figure. A, Representative SUV values across the central slice of tumors showing increased expression of PD-L1 as measured by [^{18}F]DK222 uptake before and after immunotherapy. B, Plot of [^{18}F]DK222 SUV vs distance (mm) showing increased upregulation of PD-L1 in greater proportion of the tumor and the tumor core in combination therapy treated animals than monotherapy. C, Validation using IHC showing higher PD-L1 expression in the core of combination treated tumors. D, quantification of IHC data. ****P<0.0001 by one-way ANOVA.

Conclusions: Combination therapy induced stronger PD-L1 upregulation than monotherapy alone. This difference was more evident within the core of the tumor than its periphery. Such non-invasive quantifications could help inform on the immune cell infiltration following therapies involving ICIs.

References

1. Vesely, M. D., Zhang, T. & Chen, L. Resistance Mechanisms to Anti-PD Cancer Immunotherapy. *https://doi.org/10.1146/annurev-immunol-070621-030155* **40**, 45–74 (2022).

2. Abiko, K. *et al.* IFN-γ from lymphocytes induces PD-L1 expression and promotes progression of ovarian cancer. *Br. J. Cancer* **112**, 1501–1509 (2015).

3. Lopez De Rodas, M. *et al.* Role of tumor infiltrating lymphocytes and spatial immune heterogeneity in sensitivity to PD-1 axis blockers in non-small cell lung cancer. *J. Immunother. Cancer* **10**, (2022).

4. Ferris, R. L. *et al.* Nivolumab for Recurrent Squamous-Cell Carcinoma of the Head and Neck. *N. Engl. J. Med.* **375**, 1856–1867 (2016).

5. Cohen, E. E. *et al.* Pembrolizumab (pembro) vs standard of care (SOC) for recurrent or metastatic head and neck squamous cell carcinoma (R/M HNSCC): Phase 3 KEYNOTE-040 trial. *Ann. Oncol.* **28**, v628 (2017).

6. Chatterjee, S. *et al.* A humanized antibody for imaging immune checkpoint ligand PD-L1 expression in tumors. *Oncotarget* **7**, 10215–10227 (2016).

Evaluating PD-L1 PET in assessing Immune Checkpoint Inhibitors in Cancer Therapy

Akhilesh Mishra, Kuldeep Gupta, Dhiraj Kumar, Sridhar Nimmagadda
Russell H. Morgan Department of Radiology and Radiological Sciences, Johns Hopkins University, Baltimore, MD, United States

Background: Immunotherapy using immune checkpoint inhibitors (ICIs) have significantly improved survival for certain cancers but only about 20-40% of patients receive long-term benefits[1]. To improve efficacy of ICIs, an enormous number of combination studies are being studied in the clinical trials[2]. Efficacy determination of these agents, using immune-related response criteria, require many months and no near-term pharmacodynamic endpoints are incorporated. Majority of combination therapies modulate programmed death-ligand 1 (PD-L1)[3]. PD-L1 expression is used as an indicator of increased immune cell activity early in the course of ICI therapies. PD-L1 IHC can provide information on PD-L1 positivity but it is prone to sampling errors and difficult to apply to longitudinal studies owing to dynamic nature of PD-L1[5]. Evaluating PD-L1 expression using Positron Emission Tomography (PET) imaging enables non-invasive measures at whole-body level that can overcome inherent challenges posed to IHC[6].

Objective: To validate the potential of the peptide-based PET imaging agent [^{18}F]DK222 in delineating different immune checkpoint inhibitors in cancer therapy.

Methods: A375 melanoma xenografts were established in NSG mice humanized with CD34+ cells. The mice were then divided into two groups and treated with either 5 mg/kg of anti-PD-1 (pembrolizumab) or a combination of 5 mg/kg of anti-PD-1 and 4 mg/kg of anti-CTLA-4 (ipilimumab) (n=5). [^{18}F]DK222 PET imaging was conducted before treatment initiation and 7 days after treatment commencement, while tumor growth was continuously monitored. Additionally, flow cytometry (FC) was performed to evaluate alterations in the tumor microenvironment and immune cell infiltration.

Results: PET revealed substantially higher [^{18}F]DK222 uptake from baseline in tumors of combination therapy treated mice compared to that of monotherapy **(Fig A).** FC analysis showed higher immune cell infiltration and PD-L1+ tumor cells in combination treated mice compared to monotherapy treated mice **(Fig B)**. A significant delay in tumor growth was observed with combination therapy compared to monotherapy **(Fig C)**. Change in [^{18}F]DK222 %ID/cc in monotherapy treated mice was 0.47±0.41 vs 2.90±1.89 (p=0.045) in combination treated mice **(Fig D)**. Two out of five mice with highest increase in [^{18}F]DK222 uptake in combination therapy group exhibited least tumor growth. Also, final tumor volumes negatively correlated with [^{18}F]DK222 uptake (R^2=0.33) irrespective of treatment regimen **(Fig E)**. Higher immune cells per milligram of tumor (1320 vs 230, p=0.032), PD-L1+ cells (6005 vs 2739 /mg of tumor, p=0.2557) and ratio of CD8+ to CD4+ cells (1.94 vs 0.47, p<0.0001) was observed in tumors treated with combination therapy compared with monotherapy **(Fi G)**. These results demonstrate that [^{18}F]DK222 PET has the potential to assess immunotherapy induced changes in PD-L1 levels in tumors and useful to understand responses to combination therapies early during treatment.

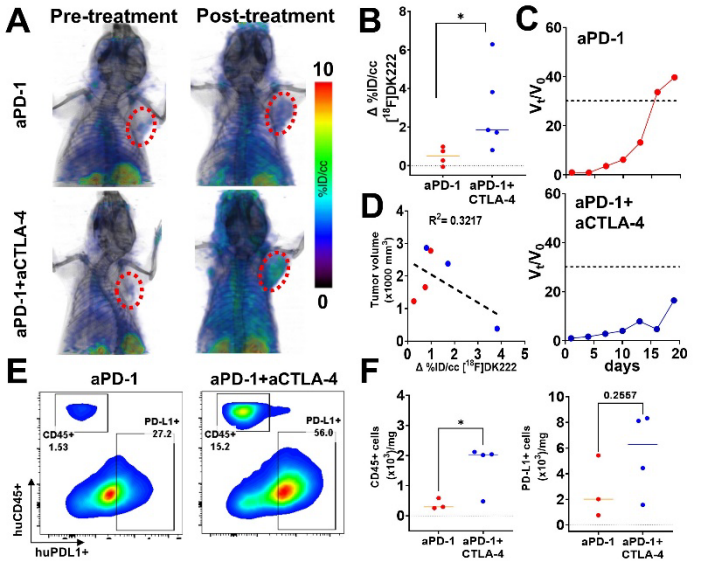

Figure. A, Representative PET images of mice receiving either monotherapy or combination therapy. Mice treated with combination therapy had increased [^{18}F]DK222 uptake. **B,** ROI analysis on tumors showing a difference in pre- and post-treatment [^{18}F]DK222 uptake between mono- and combination- therapy. **C,** Representative tumor growth curves showing reduced tumor growth in mice with high [^{18}F]DK222 uptake. **D,** Increase in [^{18}F]DK222 uptake negatively correlated with tumor growth. **F,** Representative FC data from respective mice showing increased immune cell infiltration and upregulated PD-L1 expression. *P<0.05 by student's t-test.

Conclusions: The findings indicate that [^{18}F]DK222-PET has the ability to measure fluctuating PD-L1 expression resulting from combination immunotherapy. This correlation with pathological and immunological changes suggests its potential utility in personalized treatment approaches and early-stage drug development.

References

1. Vesely, M. D., Zhang, T. & Chen, L. Resistance Mechanisms to Anti-PD Cancer Immunotherapy. *https://doi.org/10.1146/annurev-immunol-070621-030155* **40**, 45–74 (2022).

2. Galon, J. & Bruni, D. Approaches to treat immune hot, altered and cold tumours with combination immunotherapies. *Nat. Rev. Drug Discov. 2018 183* **18**, 197–218 (2019).

3. Topalian, S. L., Taube, J. M. & Pardoll, D. M. Neoadjuvant checkpoint blockade for cancer immunotherapy. *Science (80-.).* **367**, (2020).

4. Shum, B., Larkin, J. & Turajlic, S. Predictive biomarkers for response to immune checkpoint inhibition. *Semin. Cancer Biol.* **79**, 4–17 (2022).

5. McLaughlin, J. *et al.* Quantitative Assessment of the Heterogeneity of PD-L1 Expression in Non-Small-Cell Lung Cancer. *JAMA Oncol.* **2**, 46–54 (2016).

6. Chatterjee, S. *et al.* A humanized antibody for imaging immune checkpoint ligand PD-L1 expression in tumors. *Oncotarget* **7**, 10215–10227 (2016).

MPI-Guided Photothermal Therapy of Prostate Cancer using Stem Cell Delivery of Theranostic Gold-Iron Oxide Nanoflowers

Behnaz Ghaemi PhD[1], Ana Rosu BS[1], Chao Wang PhD[1], Shreyas Kuddannaya PhD[1], Gautier Laurent PhD[2], Rana Bazzi PhD[2], Stéphane Roux PhD[2], Ali Shakeri-Zadeh PhD[1], Jeff W. M. Bulte PhD[1].

[1]The Russell H. Morgan Department of Radiology and Radiological Science, Division of MR Research; and Cellular Imaging Section, Institute for Cell Engineering, The Johns Hopkins University School of Medicine, Baltimore, MD, USA.
[2]Institut UTINAM, UMR 6213 CNRS-UFC, Université de Franche-Comté, Besancon, France.

Background: Prostate cancer (PCa) is the second leading cause of cancer death in men, and it remains challenging to treat advanced PCa without damaging surrounding essential nerves. The use of theranostic nanoparticles (NPs) has been suggested for image-guided precision treatment of various cancers. However, nanoparticles often show limited distribution and retention when injected directly into tumors. Human mesenchymal stem cells (hMSCs) have been proposed as potential carriers of NPs due to their inherent tropism for tumors [1].
Objective: We investigated the efficacy of tumor-tropic hMSCs in delivering theranostic gold-decorated iron oxide nanoflowers (GIONFs) [3] to prostate tumors and whether improved retention and distribution would enhance MPI-guided photothermal therapy (PTT) ablation.
Methods: hMSCs were labeled with GIONF for 24h and evaluated with Prussian Blue staining, a Ferrozine assay, and an LDH viability assay. Tumor-tropism of labeled and unlabeled hMSCs was compared using a Boyden chamber trans-well cell migration assay. *In vitro* MPI (Momentum scanner) was performed on naked GIONFs and GIONF-labeled hMSCs. *In vivo* MPI and micro-CT were performed on DU145 (human prostate cancer)-bearing Rag2 mice injected intratumorally (i.t) with naked GIONF or GIONF-hMSCs. Mice were imaged for 7 days, and the tumor and other major organs were excised and imaged with MPI ex vivo and stained with Prussian Blue. PTT (808 nm NIR laser, 2.2 W/cm^2) was performed *in vitro* and *in vivo*. For assessment of the efficacy of *in vivo* PTT of DU145 prostate xenografts, cells were transduced with luciferase before tumor inoculation, followed by i.t. injection of GIONF-hMSCs or naked GIONF. I.t. distribution was assessed after 48 hours using MPI. The tumor was then irradiated for 7 min, and temperatures were recorded using an IR camera (FLIR-C8940, Sweden). The efficacy of tumor cell kill was assessed using pre- post-laser bioluminescence imaging (BLI).
Results: GIONF has labeled hMSCs effectively and was non-toxic up to 100 ug Fe/mL. GIONF-hMSCs retained a similar tumor-tropism/migration as unlabeled hMSCs. The *in vitro* MPI signal of GIONF-hMSCs was linear with cell number. *In vivo* MPI of prostate tumor xenografts demonstrated that tumors with i.t.-injected GIONF-hMSCs retained their original MPI signal intensity for at least 1 week, while naked GIONFs had a ten-fold reduction in signal. GIONFs from labeled hMSCs were distributed evenly throughout the tumor, but naked GIONFs had a narrow distribution along the needle track. No MPI signal was detected in off-target organs for GIONF-hMSCs, while for naked GIONFs, a weak MPI signal in the liver was seen. *In vitro* PTT studies, tumor temperature increased to 60°C, which resulted in complete ablation of DU145 tumor spheres incubated with GIONF-MSCs. *In vivo* thermometry studies of prostate xenograft tumors demonstrated an excellent efficacy of GIONF-hMSCs for PTT and BLI results confirmed cell death immediately following laser irradiation. In contrast, naked GIONF treatment achieved a maximum temperature of 46°C, with BLI signal indicating that some of the peripheral tumor cells survived treatment. Follow-up studies revealed tumor regrowth from the periphery in the naked GIONF-treated group, while no recurrence was observed in the GIONF-hMSC-treated group at 7 days post-PTT. These results highlight the superior efficacy of GIONF-hMSCs in PTT tumor ablation, attributed to their ability to distribute widely within the tumor.
Conclusions: We demonstrated the feasibility of MPI for evaluating the efficacy of GIONF-hMSCs as a theranostic intratumoral delivery system with improved intratumoral biodistribution and retention compared to naked GIONFs. Moreover, we successfully performed *in vivo* PTT using a single-shot i.t. injection of GIONF-hMSCs.

References: [1] Hao, M., et al., Adv. Funct. Mat., 32, 2201013 (2022). [3] Nicolás-Boluda, A et al., ACS Nano, 14, 5738-5753 (2020).

Establishing an efficient analysis pipeline for in vitro single cell tracking

Neha Chandra[1], Cedric Allier[2], Miroslaw Janowski[1], Piotr Walczak[1], Yajie Liang[1]
[1]Department of Diagnostic Radiology and Nuclear Medicine, University of Maryland School of Medicine, Baltimore, MD, USA; [2]Janelia Research Campus, Ashburn, VA, USA.
Corresponding author: yajie.liang@som.umaryland.edu

Background: Conventional sporadic optical imaging methods using microscopes on standard cell culture offer only a superficial glimpse of cellular morphology. Dynamic time-lapse imaging provides valuable information on cellular events such as cell cycle progression, division, or activation of signaling pathways through fluorescent sensors. For example, by effectively monitoring cell division events through longitudinal tracking of FUCCI cell cycle indicators in tumor cells, we gain critical insights into tumor progression. However, analyzing large data sizes from dynamic imaging is labor-intensive and error-prone.

Objective: We aim to establish an analysis pipeline for cell segmentation and tracking in order to enhance data analysis efficiency and gain deeper insights into dynamic cellular behaviors.

Methods: We performed long-term imaging of HEK293 expressing cell cycle indicator (FUCCI)[1] in the culture at the interval of 15 minutes for 24 hours through Tecan Spark Cyto. Then, images from three channels (bright field, green and red channels) were stacked together and registered using Linear Stack alignment with SIFT in ImageJ. The Python-based algorithm, Cellpose [3], was used for cell segmentation. To track the segmented cells over consecutive frames, the Trackmate [2] plugin on ImageJ was employed in the frame-to-frame linking ratios of 9.8, 26.1, 42.5, 58.8, and 75.2 µm (15, 40, 65, 90, and 115 pixels, respectively) encompassing a range of linking strengths to suit the varying degrees of cell movement. A subset of 10 cells was chosen for tracking analysis. The track of each selected cell was thoroughly examined and compared with the ground truth track for the first 50 frames of the time-lapse sequence. A scoring system was devised based on the number of frames in which the track correctly matched the actual cell trajectory (+1 for each correct frame). The process was done for both the brightfield and fluorescent datasets.

Results: We established a platform for long-term single-cell tracking HEK293 expressing cell cycle indicator (FUCCI). The flowchart is illustrated in **Fig. 1A**. First, cells were imaged using Tecan Spark Cyto, followed by registration. For optimized cell segmentation, we trained the models in Cellpose (**Fig. 1B**) and used them for segmentation in Trackmate. We managed to track 43 out of 114 cells with evident migration traces over 96 time-points (24 hours, **Fig. 1C**). Then we compared the accuracy of cell tracking in bright field images or integrated fluorescent intensity using different frame-to-frame linking ratios. We found the best frame-to-frame linking ratio for the fluorescent dataset was 40; however, in the brightfield dataset, 40 and 65 had similar accuracies (**Fig. 1D**).

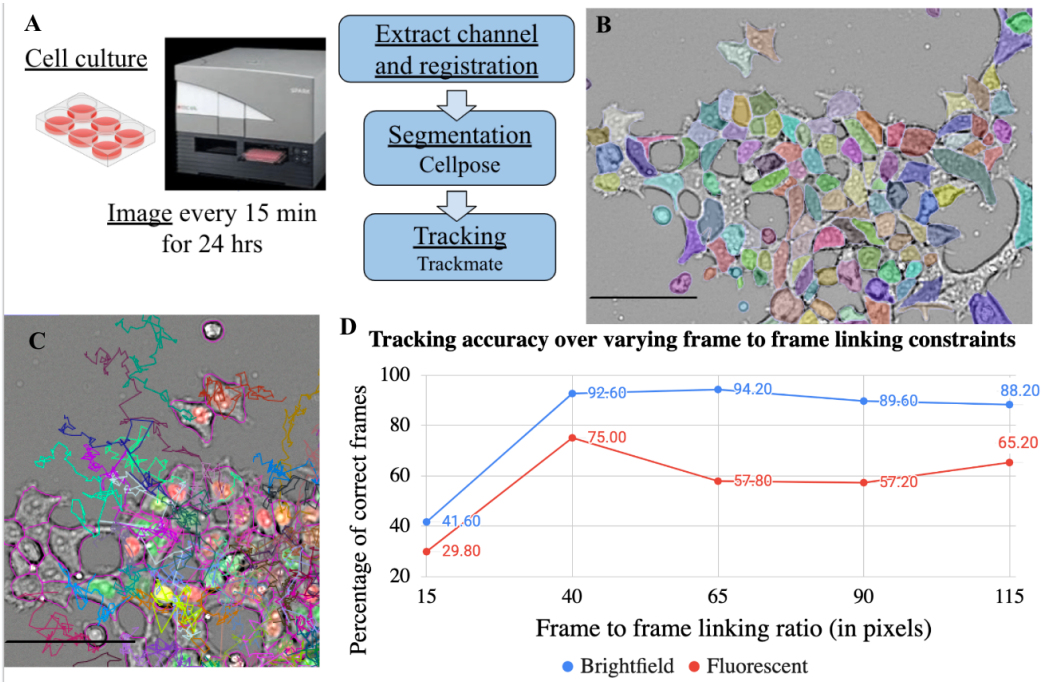

Fig. 1. **A**. Flowchart of proposed glioblastoma cell analysis. **B**. Cellpose model used for segmentation, Scale bar, 100 µm **C.** Tracks shown for snapshot of cells, Scale bar, 100 µm. **D**. Accuracy of Trackmate as measured by scoring system.

Conclusions: Our study showcases the remarkable utility of combining Cellpose with Trackmate for precise cell segmentation and tracking in quantifying dynamic cellular behaviors. The seamless integration of these advanced tools opens new possibilities for transformative advancements in understanding cell behavior.

References

[1] Chang, Y., Hellwarth, P. B., Randolph, L. N., Sun, Y., Xing, Y., Zhu, W., Lian, X. L., & Bao, X. (2020). Fluorescent indicators for continuous and lineage-specific reporting of cell-cycle phases in human pluripotent stem cells. Biotechnology and bioengineering, 117(7), 2177–2186. https://doi.org/10.1002/bit.27352

[2] Ershov, D., Phan, MS., Pylvänäinen, J.W. et al. TrackMate 7: integrating state-of-the-art segmentation algorithms into tracking pipelines. Nat Methods 19, 829–832 (2022). https://doi.org/10.1038/s41592-022-01507-1

[3] Stringer, C., Wang, T., Michaelos, M., & Pachitariu, M. (2021). Cellpose: a generalist algorithm for cellular segmentation. Nature methods, 18(1), 100–106. https://doi.org/10.1038/s41592-020-01018-x

Alavi-Bradley Symposium on Molecular Imaging and Theranostics

Suboptimal Validity of Amyloid Imaging-Based Diagnosis and Treatment of Alzheimer's Disease: Why It's Time to Abandon the Approach"

Abass Alavi, MD

Department of Radiology, Hospital of the University of Pennsylvania, Philadelphia, PA, United States

The introduction of FDG in 1976 as a biomarker for quantitative assessment of brain glucose metabolism started a paradigm shift in medicine. Since its successful synthesis, FDG-PET has been extensively employed for assessing brain function in a variety of neuropsychiatric disorders. In particular, its role in assessing patients with mild cognitive impairment (MCI) and Alzheimer's Disease (AD) has been extensively tested and validated over the past four decades. In the early 1990s, the "amyloid hypothesis" was introduced by British neuroscientists and claimed that deposition of amyloid plaque in the brain leads to MCI and eventually AD. Unfortunately, this speculative hypothesis has gained enormous power over the past three decades. Particularly, the pharmaceutical industry has invested heavily in research and potential clinical applications of the approach for both diagnosis and treatment of this common neurological disorder. While initial amyloid agents were tested with Carbon-11 labeled compounds, during the past decade, Fluorine-18 labeled amyloid tracers have been synthesized and tested in patients with suspected AD.

While the pattern of FDG uptake in the brain exactly matches histologic results of the brains of AD patients, those of amyloid PET imaging substantially differ from what is known about the distribution pattern of amyloid plaques. As such, concerns have been raised about the validity of amyloid imaging for accurate diagnosis of patients with MCI and AD.

During the past decade, several anti-amyloid antibodies have been introduced and tested in human beings with controversial results. While initial trials failed to show evidence for cognitive improvement in this population, recently, claims have been made about a substantial role for its efficacy in patients with this serious and disabling neurological disorder.

While there are serious concerns about the validity of amyloid imaging for optimal management of patients with AD, serious issues have also been raised about a lack of efficacy and toxicity of anti-amyloid treatments. In particular, improvement following these treatments is questionable, and therefore, there is an ongoing debate whether such treatments are justifiable based on the existing data. MRI scans of patients who have received anti-amyloid antibodies show significant amyloid related imaging abnormalities (ARIAs). Very likely, these structural abnormalities lead to significant brain dysfunction, and therefore, the routine use of such treatments is of serious concern among physicians who treat and manage AD patients. Similarly, these patients develop significant brain atrophy over time which is an indication of irreversible damage to the brain structures by such treatments. In conclusion, FDG-PET remains the study of choice for diagnosis of MCI and AD. As such, the roles of amyloid-based diagnosis and treatment are questionable at this time.

The Role of FDG-PET in Assessing Age-Related Regional Brain Metabolism Changes

Chitra Parikh BA[1], Eric M. Teichner BA[1], Robert C. Subtirelu MSc[2], Connor R. Crutchfield BA[1], Victoria A. Anderson BA[1], Sahithi Talasila BS[1], Arjun B. Ashok BA[1], Poul Flemming Høilund-Carlsen MD PhD[3], Mona-Elisabeth Revheim MD PhD,[4] Thomas J. Werner MSE[2], Abass Alavi MD[2]

[1]Sidney Kimmel Medical College, Thomas Jefferson University, Philadelphia, PA
[2]Department of Radiology, Hospital of the University of Pennsylvania, Philadelphia, PA
[3]Department of Nuclear Medicine, Odense University Hospital, 5000 Odense C, Denmark
[4]Institute of Clinical Medicine, University of Oslo, Oslo, Norway

Background: Understanding the differences in regional brain metabolism that occur with aging improves our ability to diagnose and treat age-related neurological disorders. The development of possible biomarkers and future therapies for neurodegenerative diseases hinges on the understanding of age-related changes in a healthy population. Aging alters cognitive function even in the absence of recognizable structural changes and can be detected using modern in vivo functional imaging modalities such as ^{18}F-fluorodeoxyglucose positron emission tomography (FDG-PET).

Objective: This study aimed to analyze glucose metabolism within nine brain regions in order to record the changes in metabolism associated with normal aging. In doing so, this study aimed to understand the utility of FDG-PET in the measurement of age-related metabolism changes.

Methods: In total, 79 subjects (with a mean age of 44.5 ± 13.8 years) were included (46.8% females, 53.2% males). Subjects had a negative history of cancer, chronic inflammatory disease, autoimmune disease, immunodeficiency syndromes, alcohol abuse, illicit drug use, any prescription drug use, and cardiovascular disease (CVD). All subjects underwent whole-body FDG-PET/CT imaging 180 minutes after the administration of 4.0 MBq/kg dose of FDG. The quantitative regional analysis of PET images was performed using MIMneuro version 7.1.5 (MIM Software, Inc., Cleveland, Ohio). Acquired PET data was normalized to injected dose and body weight to produce standardized uptake value (SUV) images. Individual SUVmean for the brain stem, the cerebellum, the frontal lobe, the lateral temporal lobe, the medial temporal lobe, the occipital lobe, the parietal lobe, the temporal lobe, and the thalamus were recorded. Pearson's R was calculated and evaluated for significance in all variables. The threshold for significance was set at $P < 0.05$.

Results: Various significant associations between age and FDG uptake across all nine brain regions of interest were observed. In particular, age was found to have an inverse correlation with regional metabolism in the brainstem ($r= -0.323$, $p= 0.004$), cerebellum ($r= -0.338$, $p= 0.002$), frontal lobe ($r= -0.463$, $p < 0.001$), lateral temporal lobe ($r= -0.436$, $p< 0.001$), medial temporal lobe ($r= -0.384$, $p< 0.001$), occipital lobe ($r= -0.392$, $p< 0.001$), parietal lobe ($r= -0.453$, $p< 0.001$), temporal lobe ($r= -0.427$, $p< 0.001$), and thalamus ($r= -0.321$, $p= 0.004$) among healthy individuals.

Conclusions: The results demonstrate a significant age-dependent reduction of ^{18}F-FDG uptake in the brain among healthy individuals. Research regarding the phenotypical, metabolic, and physiological changes that occur in healthy individuals allows us to better recognize and understand neurological disease states. The observed changes in glucose metabolism, as measured by FDG-PET imaging, were significant and consistent across all nine brain regions. This study highlights the value of modern functional imaging techniques, such as FDG-PET, in understanding the effects of normal aging on the brain and may serve as a useful foundation for future research in this area.

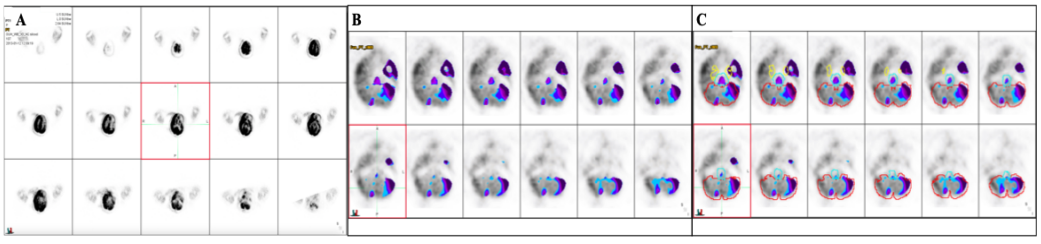

Figure 1. Quantitative assessment of FDG-PET/CT slices interpreted by MIMNeuro. (**A**) Grayscale axial views of FDG-PET/CT. (**B**) PET/CT shows low FDG uptake, represented by purple and blue contours, in several critical regions. (**C**) FDG-PET/CT shows low uptake in the medial temporal lobe (*yellow*), cerebellum (*red*), and brainstem (*blue*).

Development of HIV-neutralizing antibody-producing cells.

Lorissa McDougall[1],MSc, Abdolrahim Abassi[2], PhD, Mohammad Sajadi[2], PhD, Alonso Heredia[2], PhD, Linda Chang[1], MD, Yajie Liang[1], PhD, Chengyan Chu[1], PhD, Miroslaw Janowski[1], MD PhD, Piotr Walczak[1], MD PhD.

[1]University of Maryland, Baltimore, Department of Radiology and Nuclear Medicine; [2]University of Maryland, Baltimore, Institute of Human Virology.

Background and objective: The human immunodeficiency virus (HIV) affects around 1.2 million people in the United States, with prevalence rates impacted by ethnicity, gender, and age. The detection and treatment of HIV has vastly improved in recent years. The virus no longer shortens life expectancy; with a mortality rate of only 2% in infected people [1]. However, persons with HIV (PWH) are dependent on lifelong antiretroviral medications due to persistent infection from viral reservoirs in the brain, which can lead to re-infection in the host upon drug cessation[2]. Therefore, this project aims to eradicate HIV from the brain by transplanting genetically engineered glial progenitor cells (GRPs) that express a neutralizing antibody (bNAb) against the envelope protein of HIV. The modified cells will be delivered to humanized mice infected with HIV *via* intraarterial (IA) injection, where they migrate through the blood into the brain. In the brain, they will produce the antibody, which, when bound to the HIV envelope, will trigger an immune response against HIV, ultimately clearing the infection and reducing the need for long-term treatments.

Methods: Transfection of the HIV bNAb constructs was optimised in HEK293 cells by incubating the cultures with 500ng of GFP expressing HIV bNAb constructs (CII and CIII), lipofectamine 2000, and optiMEM over 48 hours, at which point the supernatant was collected for ELISA and the cells were imaged for transfection efficiency. Once we observed reliable transfections and HIV bNAb production, we packaged the constructs by 2nd generation lentiviral packaging, using the psPAX2 packaging plasmid and pMD2G envelope plasmid. The virus, including the constructs, was harvested and concentrated to be used for transduction. A successful transduction of the virus with polybrene over 48 hours was confirmed by flow cytometry.

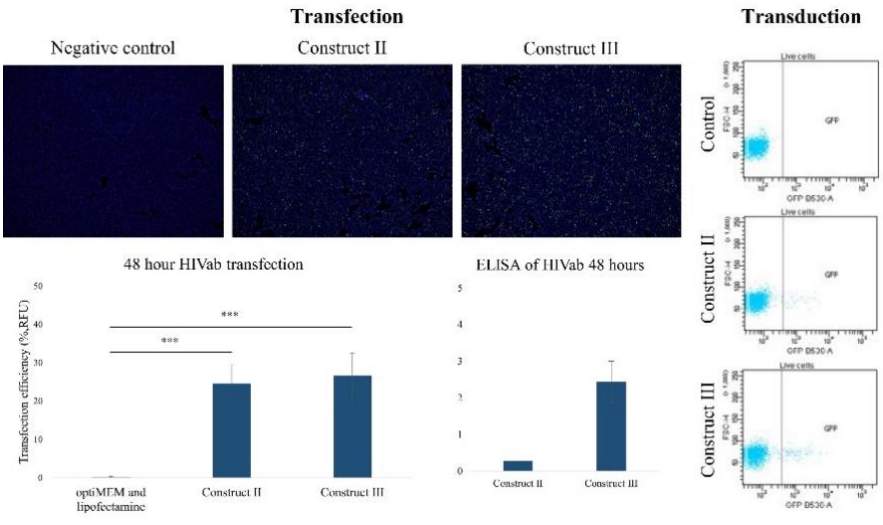

Results: We found that after 48 hours of transfection, an average of 25% and 27% GFP-positive cells were found in the CII and CIII cultures, respectively. Additionally, the supernatant from these populations showed antibody binding in ELISA assays. Furthermore, these constructs were packaged for transduction from which we isolated GFP-positive cell populations *via* flow cytometry.

Conclusions: We successfully modified HEK293 cells to produce a stable cell line as a benchmark for future applications of bNAb construct to GRPs.

Figure: Transfection of CII and CIII in HEK293 cultures showed a significant increase from the negative control as well as production of HIV bNAb as detected by ELISA. Transduction of these constructs has also produced GFP-positive populations in these cells.

Acknowledgements: This work was supported by grants from the NIH (R01DA056739-02; DP1-DA053719-03)

References: [1] Maureen R. Benjamins, Nazia Saiyed, Samuel Bunting, Peter Lorenz, Bijou Hunt, Nancy Glick & Abigail Silva. HIV mortality across the 30 largest U.S. cities: assessing overall trends and racial inequities, *AIDS Care* 2022 34:7, 916-925, https://doi.org/10.1080/09540121.2021.1939849.

[2] Ash, M.K.; Al-Harthi, L.; Schneider, J.R. HIV in the Brain: Identifying Viral Reservoirs and Addressing the Challenges of an HIV Cure. *Vaccines* 2021, *9*, 867. https://doi.org/10.3390/vaccines9080867.

PET NANO-RADIOTRACERS FOR TARGETED NEUTROPHIL DETECTION IN PULMONARY ARTERIAL HYPERTENSION

Dr. Lucía Fadón-Padilla,[a,b,f] Dr. Ana Beatriz Miguel-Coello[a] Marta Beraza-Cabrerizo [a] Desiré Di Silvo [a] Ainhize Urkola-Arsuaga [a] María Jesús Sánchez-Guisado [a,c] Irati Aiestaran-Zelaia [a,d] Dr. Edurne Berra [b] Dr. Susana Carregal-Romero*[a,c,d] and Professor Jesús Ruíz-Cabello*[a,c,d,e]

[a] Center for Cooperative Research in Biomaterials (CIC biomaGUNE). Donostia, Spain
[b] Center for Cooperative Research in Bioscience (CIC bioGUNE). Derio, Spain
[c] Centro de investigación en red de enfermedades respiratorias (CIBERES). Madrid, Spain
[d] Biodonostia Health Research Institute. Donostia, Spain
[e] Ikerbasque, Basque Foundation for Science. Bilbao, Spain
[e] Universidad Complutense de Madrid. Madrid, Spain
[f] University of Maryland. Baltimore, MD, United States

Background

Pulmonary arterial hypertension (PAH) is a severe disease characterized by increased blood pressure in the pulmonary artery that can ultimately damage the heart's right ventricle. PAH presents pathophysiological heterogeneities that make its early diagnosis and treatment difficult. This highlights an urgent need for molecular probes that can help in both developing effective diagnostic tools and personalized medicine.

Objective

This study explored the potential of nano-radiotracers based on ultrasmall iron oxide nanoparticles, that were functionalized with the N-cinnamoyl-F-(D)L-F peptide, to detect an increase in neutrophil population in the context of PAH.

Methods

We compared the specificity of ^{68}Ga-IONP-citrate-cFLFLF radiotracer with the widely used probe ^{18}F-Fluorodeoxyglucose in two rat models of PAH with different profiles of inflammation and neutrophil infiltration, the monocrotaline (MCT) induced model, and hypoxia plus sugen (SuHx) model.

Results

Both PAH models demonstrated right ventricular hypertrophy and remodeling of the pulmonary vasculature, although only the MCT rats coursed with accumulation of neutrophils in the lungs, demonstrated by an increase in the uptake of our radiotracer and verified by histology. The uptake of ^{18}F-fluorodeoxyglucose did not prove to be related to the accumulation of neutrophils.

Conclusions

Our findings provided promising results regarding the use of ^{68}Ga-IONP-citrate-cFLFLF as a nano-radiotracer for targeted detection of neutrophils, suggesting that this nanoprobe can be used to investigate cell-specific inflammatory processes as secondary hit causing the differences observed in RV heart failure and vascular wall remodeling in PAH. Our histological data supports the direct link of neutrophils and nano-radiotracer accumulation in the lung of MCT animals. Our also demonstrated that our nanoprobes are superior to ^{18}F-Fluorodeoxyglucose in detecting an increase in neutrophil population and inflammation, highlighting the feasibility of using rational design of nanoprobes to enhance current medical diagnostic tools.

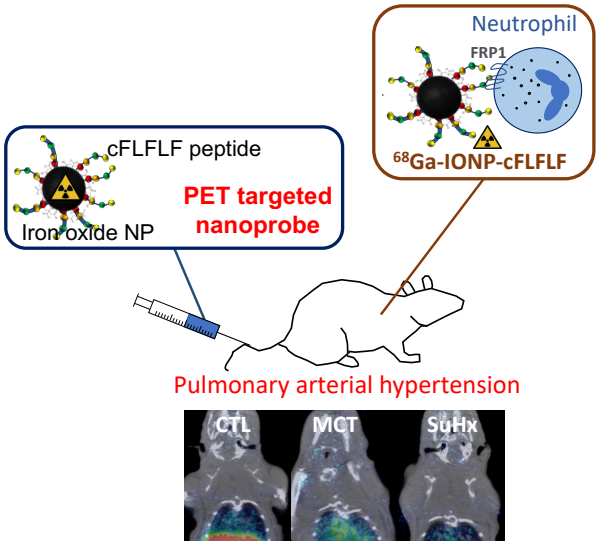

Investigation of Glutamine Utilization in Prostate Cancer Xenografts using MALDI Imaging

Caitlin M. Tressler, Ph.D.[1], Natalie Dillman[1], Behnaz Ghaemi, Ph.D.[1,2], Jeff W.M. Bulte, Ph.D.[1,2], Aline M. Thomas, Ph.D.[1,2]

[1]Russell H. Morgan Department of Radiology and Radiological Science and [2]Institute for Cell Engineering, Johns Hopkins University School of Medicine.

Background: Glutamine dependence is an attractive target for cancer imaging and therapy. Upon transport into the cell, it is metabolized for energy and bio-synthesis[1]. ASCT2, the primary transporter for glutamine, and GLS1, the primary enzyme that converts glutamine to glutamate, are associated with poor prognosis for many cancers and are targets of drugs currently in clinical trials. More recently, abnormalities in downstream glutaminolysis proteins have been identified. Mass spectrometry imaging can detect many metabolites through their molecular mass while preserving their spatial distribution. Furthermore, the low ionization energy of MALDI (matrix-assisted laser desorption/ionization) imaging permits co-registration of metabolic information with histological images[2] of tissues, which are routinely collected in the clinic. **Objective:** Previous investigations of glutamine metabolism in tumors using mass spectrometry imaging evaluated steady-state concentrations[3]. We extended these studies by imaging after the administration of $^{13}C5,^{15}N2$-glutamine, which permits evaluation of metabolic flux through the tracing of isotopically-substituted metabolites. **Methods:** We evaluated glutamine metabolism in human prostate tumor xenograft models. DU145 (n=6) and LNCaP (n=8) prostate cancer cell lines were injected subcutaneously into immunodeficient Rag2 mice. Glutamine (6 mmole/kg) was intravenously injected 1-2 months after tumor induction. Seventy-five minutes after injection, tumors were excised for imaging. Tumors were cryosectioned (10 µm thick) onto indium tin oxide slides. Four passes of 10mg/10mL 1,5-diaminophthlene in 70% acetonitrile with 0.1% were applied. MALDI images were obtained using a Bruker Rapiflex MALDI-TOF/TOF mass spectrometer in reflection negative mode with a 100x200 µm raster. **Results**: Metabolites screened included injected $^{13}C5,^{15}N2$-glutamine and downstream metabolites: $^{13}C5,^{15}N$-glutamate, $^{13}C5$-α-ketoglutarate, ^{15}N-alanine, ^{15}N-aspartic acid, ^{15}N-glycine. Also screened were cysteine, cystine, leucine, pyruvate, oxaloacetate, and NADPH. Isotopomer analysis revealed a higher presence of $^{13}C5,^{15}N2$-glutamine/$^{13}C5,^{15}N$-glutamate and ^{13}C-labeled α-ketoglutarate in LNCaP tumors compared to DU-145 tumors. Leucine, cysteine, and NADPH were also present in greater quantities in LNCaP tumors. **Conclusion:** This study preliminarily demonstrates using xenograft prostate cancer models that differences in glutamine utilization can be detected *ex vivo* with injection of $^{13}C5,^{15}N2$-glutamine and MALDI images of stable isotope-containing metabolites.

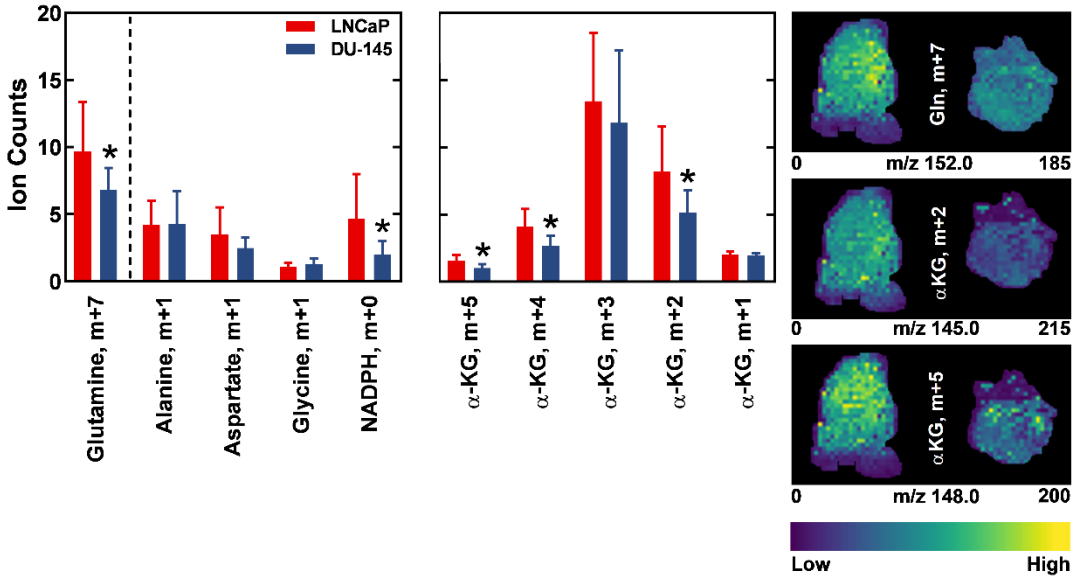

Figure 1. Presence of metabolites in xenograft prostate tumors 75 minutes after intravenous injection of $^{13}C5,^{15}N2$-glutamine. The shift in mass due to the presence of stable isotopes is indicated as m+x. *=p<0.05 between LNCaP and DU145 tumors. Gln=glutamine. αKG=α-ketoglutarate.

References: (**1**) Choi YK and Park KG. Targeting Glutamine Metabolism for Cancer Treatment. Biomol Ther (Seoul). 2018;26(1):19-28. (**2**) Chughtai K, et. al. Fiducial markers for combined 3-dimensional mass spectrometric and optical tissue imaging. Anal Chem. 2012;84(4):1817-23. (**3**) Andersen MK, et al. Spatial differentiation of metabolism in prostate cancer tissue by MALDI-TOF MSI. Cancer & Metabolism. 2021;9(1):9.

Acknowledgements: MALDI imaging experiments were performed in the Johns Hopkins Applied Imaging Mass Spectrometry (AIMS) Core facility. **Funding:** NIH (K01EB030612, R01EB030376).

Application of Metabolic Imaging of Hyperpolarized [1-^{13}C]Pyruvate to a Genetic Mouse Model of Nonalcoholic Steatohepatitis

Aditya Jhajharia[1], Salaheldeen Elsaid[1], Minjie Zhu[1], Joshua Rogers[1], Youngshim Choi[2], Liqing Yu[2], Sui Seng Tee[1], Dirk Mayer[1]

[1]Department of Diagnostic Radiology and Nuclear Medicine, University of Maryland, Baltimore, USA. [2]Department of Medicine, University of Maryland, Baltimore, USA.

Background: Nonalcoholic fatty liver disease (NAFLD) is the most common chronic liver disease and can progress to a more severe form called nonalcoholic steatohepatitis (NASH). The current gold standard for NASH diagnosis is liver biopsy – an invasive procedure associated with complications in up to 5% of patients and subject to sampling errors. Therefore, a noninvasive method to differentiate NASH from steatosis is an unmet clinical need.

Objective: We aim to explore if hyperpolarized (HP) [1-^{13}C]pyruvate magnetic resonance spectroscopic imaging (hpMRSI) can detect metabolic differences in a genetically engineered mouse model of NASH.

Methods: The comparative gene identification 58 (CGI-58) knockout (LivKO) mouse model of NASH was used and CGI-58-floxed mice used as controls. A clinical 3 T GE 750w MRI scanner (GE Healthcare, Waukesha, WI, USA) was used to acquire HP metabolic imaging data using a 3D spiral chemical shift imaging (spCSI) sequence. Liver tissues were processed for hematoxylin and eosin (H&E) staining for histology evaluation.

Results and Conclusions: The histology evaluation of the control mice showed normal liver histology with no or minimal background inflammation, and no necrosis or fibrosis. In contrast NASH mice showed a wide range of inflammation, necrosis, and steatosis. We categorized them as mild, moderate and severe stages according to injury level observed in histology. LivKO mice with severe liver injury showed significantly higher pyruvate (Pyr) to lactate (Lac) and Pyr to alanine (Ala) conversion in liver compared to control mice. We observed a trend in increasing Pyr to Ala conversion depending on the level of liver injury. This progression could potentially provide valuable insights into the advancement of the disease. These results indicate the potential of the method as a noninvasive clinical tool to differentiate between NAFLD and NASH.

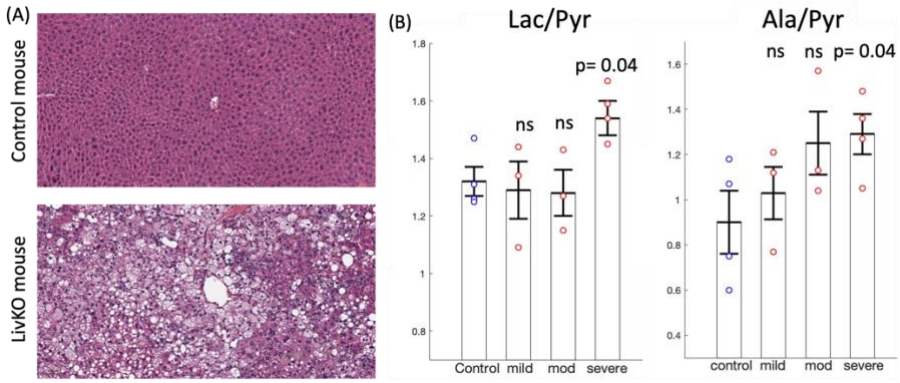

Fig. (A) A representative micrograph of liver stained with H&E showing the central vein (top left); and LivKO mice (bottom left). (B) Average Lac-to-Pyr (left), and Ala-to-Pyr (right) ratios for control, NASH mice with mild, moderate, and severe injury (left to right) with standard errors and individual values (control, severe: N=4; mild, moderate: N=3).

Application of L+S reconstruction with local sparsity to dynamic hyperpolarized ^{13}C spiral chemical shift imaging in-vivo

Minjie Zhu, M.Sc., Aditya Jhajharia, Ph.D., Joshua Rogers, M.Eng., Dirk Mayer, Dr. rer. nat.
Diagnostic Radiology & Nuclear Medicine, University of Maryland School of Medicine, Baltimore, MD, USA

Background Due to the non-recoverable nature of the magnetization fast acquisition scheme are important in metabolic imaging of hyperpolarized substrates. Acceleration for dynamic Spiral Chemical Shift Imaging (spCSI) [1] can be achieved through under-sampling the spiral k-space by acquiring a subset of the full interleaves. Direct inverse image reconstruction using conjugate gradient (CG) method on the under-sampled data will induce image artifacts. These artifacts can be removed via iterative reconstruction with low-rank (L) plus sparse (S) matrix decomposition model (L+S) [2]. In a previous application, iterative soft thresholding of the L and S matrices was applied to the entire spectro-spatio-temporal matrix respectively, represented as global low rank and global sparsity (GLGS). Since the high-intensity pyruvate contributes the majority of the MR signal, threshold of the sparsity matrix is set according to the features of pyruvate. As a result, features of the lower intensity components (lactate and alanine) are dominated by pyruvate, inducing distortions in the dynamic pattern of the metabolic products.

Objective

The goal of this study is to reconstruct under-sampled dynamic images with no significant image artifacts and distortions in dynamic patterns for all metabolites.

Methods

Spectroscopic imaging features 'local sparse' property as neighboring spatial components have similar dynamics after the sparse transform, but each frequency component may not share the same dynamic pattern. In analogy to the local low rank application by Milshteyn et al [3], we apply a global low rank plus local sparse reconstruction (GLLS) using multiple blocks along the spectral dimension with thresholds set for each block individually, thus retaining each frequency component's dynamic pattern. In-vivo imaging was performed on a healthy mouse with injection of hyperpolarized pyruvate. Under-sampled spCSI data was acquired by pseudo-randomly selecting 8 out of 24 spiral interleaves at each time frame, with every 3 time frames forming a fully sampled k-space block. Dynamic images at 3 seconds temporal resolution can be reconstructed with direct inverse on the fully sampled blocks (CG, R=1), whereas dynamic images at 1 second temporal resolution can be reconstructed using the under-sampled data via direct inverse (CG), GLGS and GLLS at 3 fold acceleration (R=3).

Results

Dynamic images for pyruvate, lactate and alanine are reconstructed from the acquired spCSI data using the four methods mentioned above, shown in Figure 1. Accelerated images with direct inverse reconstruction (CG,R=3) display significant image artifacts due to under-sampling. Both GLGS and GLLS can effectively reduce the image artifacts for all three metabolites. Reference to the results reconstructed from fully sampled data (CG, R=1), attenuation in lactate and alanine intensity are seen in later time frames (14s and 15s) with GLGS. The plotted dynamic curves also represent the distorted lactate and alanine pattern for GLGS. In contrast, no apparent distortions in the time course of the metabolic products are found in the results reconstructed with GLLS.

Conclusion

GLLS can successfully reconstruct under-sampled dynamic spectroscopic imaging data without significant artifacts and properly restore the distinct dynamic pattern of lower intensity metabolites. Thus, effective imaging acceleration can be achieved.

References [1] Mayer, Dirk, et al. Magn Reson Med 2006, 932-937. [2] Otazo, Ricardo, et al. Magn Reson Med 2015, 1125-1136. [3] Milshteyn, Eugene, et al. Journal Magn Reson 2018, 46-59

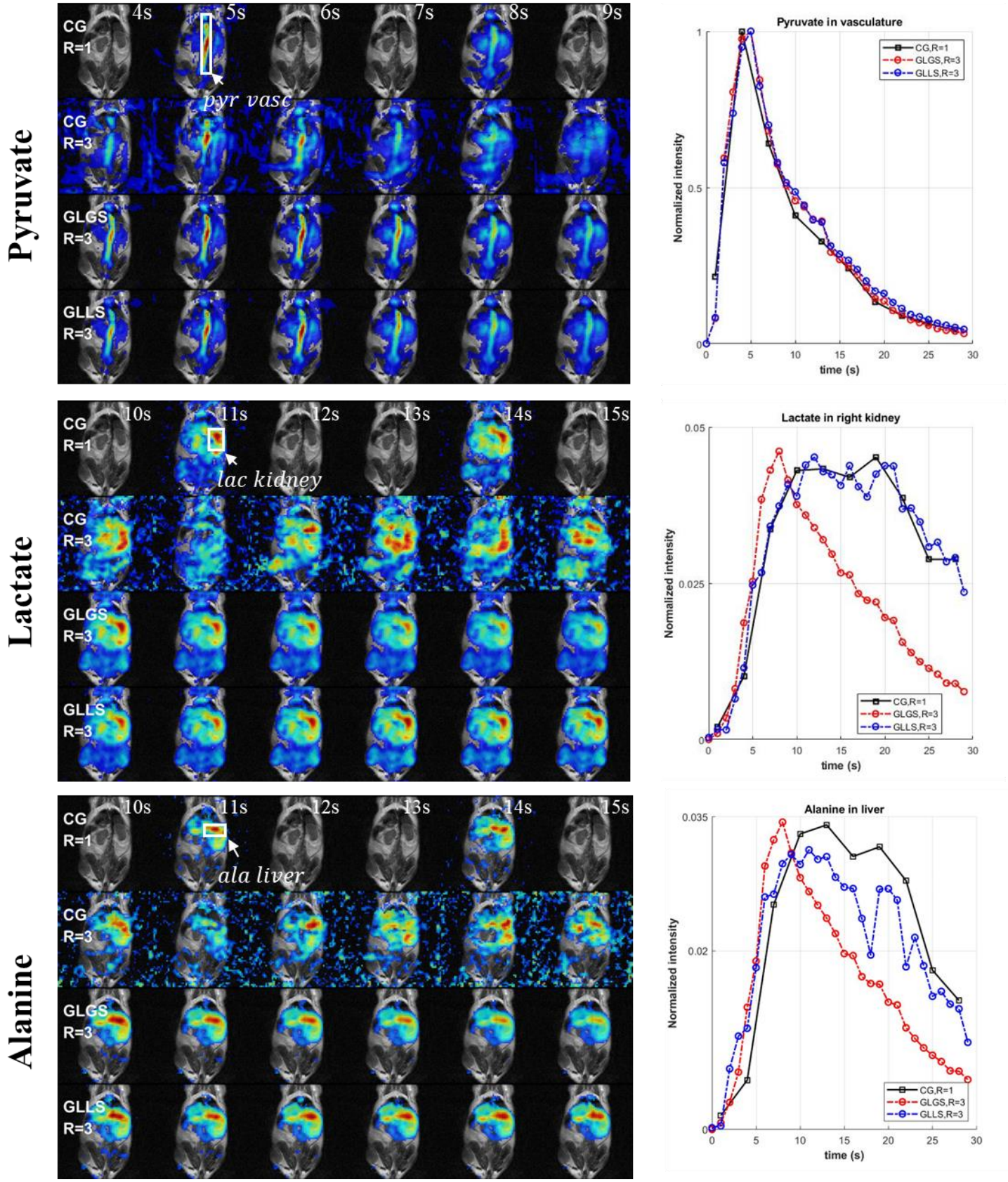

Figure 1. Dynamic images of the 2D coronal mouse body imaging reconstructed with 4 methods at selected time frames: direct inverse on fully sampled k-space (CG,R=1); direct inverse on under-sampled k-space (CG,R=3); Global low rank plus global sparsity (GLGS, R=3); Global low rank plus local sparsity (GLLS, R=3); Dynamic curves are plotted for the selected ROI (white rectangle) for each metabolite

Bimodal (MRI/two-photon microscopy) mouse brain imaging using a modular cranial attachment system

Colleen Russell, Mikolaj Walczak, Guanda Qiao MD, Miroslaw Janowski MD, PhD, Piotr Walczak MD, PhD, Yajie Liang MD, PhD

Department of Diagnostic Radiology and Nuclear Medicine, School of Medicine, University of Maryland Baltimore

Background. Two-photon microscopy (2PM) is widely used to study the brain at a high spatial and temporal resolution but at the cost of limited spatial coverage. In contrast, MRI provides large-scale visualization of the brain, but its resolution is limited. The dual modality of 2PM and MRI imaging of the same subject solves these problems by yielding high-resolution and large-scale visualization of anatomical structures and physiological processes. However, traditional metallic head fixation devices for 2PM *in vivo* brain imaging cannot be used in conjunction with MRI due to image artifacts, so an MRI-compatible head fixation system is needed.

Objective. The development of a modular cranial attachment system enabling MRI and 2PM bimodal imaging.

Methods. We designed a dual-component system: a metal head bar with internal M8 threads and a 3D-printed base featuring external threads. The base will be permanently attached to the mouse skull via adhesives, while the metal head bar is thread-fixed to the base solely during 2PM imaging. Using the high-resolution ELEGOO Mars 2 3D printer, we printed the base component's M8 threads (0.5 mm pitch, 8 mm outer diameter, 6.6 mm inner diameter). The base height is designed for flush head bar placement on the skull. We added M8 threading inside to match the 3D printed base by modifying an existing head bar model. Supports were added to ensure successful printing. The .stl design file is sliced into .ctb format via CHITUBOX for Mars 2 printing. We used resin-printed to scale mouse skull models with 0.6% agarose-filled cranial cavities injected with a 4:1 fluorescent bead-iron oxide mixture (FBIO) for MRI contrast and TP microscopy visibility to test the attachment system. A cranial window is placed between the gel and adapter, adhered to the skull.

Results. Our newly designed head fixation system consists of two parts attached to a skull: a base and a removable head bar (**Fig. 1A**). We designed the base (**Fig. 1B**) using Tinkercad and printed it with the ELEGOO Mars 2. The head bar was ordered from eMachineShop in aluminum with M8 threads that fit the base (**Fig. 1C**). The resin-printed head fixation adapter is durable and can withstand the force the head bar inflicts when fastened. The FBIO was injected into 0.6% agarose gel at 500 µm depth (**Fig. 1D**). The adapter also fits the skull topography as intended after being glued on. In the MRI, the only element of the head fixation system is the base which did not interfere with the model's anatomical accuracy or positioning stability (**Fig. 1E**). With the head fixation system assembled; the skull fits seamlessly into the experimental configuration station for the 2PM device (**Fig. 1F**). The MRI signals (T1) identified that the agarose gel could be observed clearly along with the FBIO injected 500 µm below the surface of the agarose. The adapter did not cause interference in the signals obtained (**Fig. 1G**). The agarose gel injected with FBIO at 500 µm was also observed under the 2PM, and a 3D stack was rendered from the sliced data images (**Fig. 1H**).

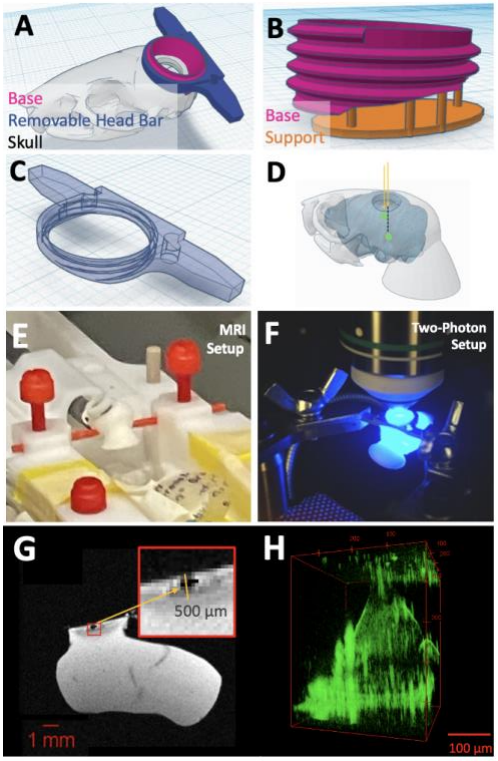

Figure 1. (**A**) Modular cranial attachment system. (**B**) Close-up of M8 screw fixation on mouse skull with supports for printing. (**C**) Two-photon fixation head bar model. (**D**) Schematic of stereotactic injection of FBIO into mouse brain model. (**E**) Positioning of mouse skull for MRI. (**F**) Two-photon head fixation setup for imaging. (**G**) T1 MRI scan of 500 µm-deep injection of FBIO in mouse brain model. (**H**) Side-view of 3D reconstruction of the 500 µm-deep injection site using 2PM slices. 1 mm grid squares for **A**, **B**, and **C**.

Conclusion. The resin-made 3D-printed adapter for the modular head fixation system was successful in its functionality for bimodal imaging (2PM and MRI scanning). We observed the same structure under the 2PM and MRI, which justifies testing in live animals.

A Review of The Role of FDG-PET in the Diagnosis and Management of Hidradenitis Suppurativa

Sahithi Talasila[1], Eric M. Teichner[1], Robert C. Subtirelu[2], David H. Xiang[3], Cyrus Ayubcha[3,4], Thomas Werner[2], Abass Alavi[2], Mona-Elisabeth Revheim[5,6]

1. Sidney Kimmel Medical College, Thomas Jefferson University, Philadelphia, PA.
2. Department of Radiology, Hospital of the University of Pennsylvania, Philadelphia, PA.
3. Harvard Medical School, Boston, MA
4. Department of Epidemiology, Harvard Chan School of Public Health, Boston, MA, USA
5. The Intervention Centre, Division of Technology and Innovation, Oslo University Hospital, Oslo, Norway.
6. Institute of Clinical Medicine, University of Oslo, Oslo, Norway

Abstract

Background:

Hidradenitis suppurativa (HS) is a chronic skin disorder characterized by nodules, comedones, and sinus tracts that often leave prominent scarring. In recent years, non-invasive imaging techniques have been used to assess the inflammatory activity, vascularization, and treatment response of lesions. Specifically, fluorine-18 fluorodeoxyglucose positron emission tomography/computed tomography (FDG-PET/CT) scans may aid in identifying systemic inflammation in patients with HS, improving diagnosis. Inflamed hypermetabolic tissues exhibit greater uptake of FDG due to increased glucose uptake and vascularity.

Objective:

A systematic review was conducted to summarize the utility of nuclear imaging techniques in the diagnosis and treatment follow-up of HS.

Methods:

PubMed, Scopus, and ScienceDirect databases were utilized for relevant articles discussing the utility of PET scans in managing HS. A total of 51 citations were identified in the initial search. Following the review of titles, abstracts, and duplicates, 43 articles were excluded, leaving a total of eight articles for. Data were extracted from each article, encompassing the number of patients, imaging techniques employed, and final results.

Results and Conclusions:

Analysis of the data demonstrated that FDG-PET showed evidence of identifying subclinical lesions of the disease, improving the visualization of HS, and providing an objective method of assessing severity.

Key Words: Hidradenitis suppurativa, non-invasive imaging techniques, fluorine-18 fluorodeoxyglucose, FDG-PET/CT, systemic inflammation, diagnosis, treatment follow-up, SAPHO syndrome

Automatic Two-Photon Imaging Platform (ATPIP) for Longitudinal Cell Tracking

Mikolaj Walczak, Colleen Russell, Miroslaw Janowski MD, PhD, Piotr Walczak MD, PhD, Yajie Liang MD, PhD

Department of Diagnostic Radiology and Nuclear Medicine, School of Medicine, University of Maryland at Baltimore

Background. Single cell tracking is a powerful tool which aids in understanding cellular functions [1]. Using two-photon (TP) microscopy along with fluorescent labeling, the morphology, migration, cell cycle, and signaling pathways of live cells can be observed. However, it is highly labor intensive to manually acquire images under multiple wavelengths using current software. This makes it almost impossible to track cells over extended periods of time using fixed short intervals for various fluorescent indicators at their corresponding excitation wavelengths.

Objective. To automate the control of both TP laser and microscope for programmable acquisition of spectral and timelapse information from live cells.

Methods. ScanImage controls the microscope for image acquisition through MATLAB while Chameleon GUI communicates with the Chameleon Discovery laser. HEK293 cells were transduced by lenti-EF1a-FUCCI (Fluorescent Ubiquitination-based Cell Cycle Indicator)-PAGFP (Photoactivatable Green Fluorescent Protein)-RGECO (Red Calcium Indicator) and imaged without environment control using a water immersion Olympus 25x objective with a numerical aperture of 1.05 and zoom of 2x. The experiment was conducted using a total stack height of 30 µm with slices every 2 µm. The imaging rate is 30 Hz averaging 60 frames into one frame.

Result. ATPIP was programmed in MATLAB and designed for executing the following four functions. First, a laser communication scheme was used to control the laser and took the place of the Chameleon GUI (**Fig. 1a, I**). Second, it coordinated between the laser and ScanImage to select the desired laser wavelengths and adjusted the laser power for the 3D stack acquisition at specified timepoints (**Fig. 1a, II**). Third, it scheduled scans at fixed intervals for a desired total time to achieve longitudinal cell tracking (**Fig. 1a, III**). Finally, it generated a timelapse of the 3D stack acquisition at each timepoint to allow for functional imaging at a pre-selected slice (**Fig. 1a, IV**). As a proof-of-concept experiment, we chose to view the HEK293 sample under wavelengths of 800 nm and 940 nm for a duration of four hours with a scan interval of fifteen minutes (**Fig. 1b left panel**). 800 nm excitation excites fluorescent proteins in FUCCI to indicate cell cycle progression (**Fig. 1b center panel**). We photoactivated PAGFP of a single cell under 800 nm for 1 minute and used a 940 nm excitation for cell tracking (**Fig. 1b right panel**). After running the imaging session, we used Cellpose [2] for cell segmentation and TrackMate [3] to identify the pathing of individual cells (**Fig. 1c left panel**). We found clear tracks of the cells that express FUCCI under 800 nm throughout the four-hour period and analyzed the florescent signal intensity for both the red and green channels (**Fig. 1c center and right panels**).

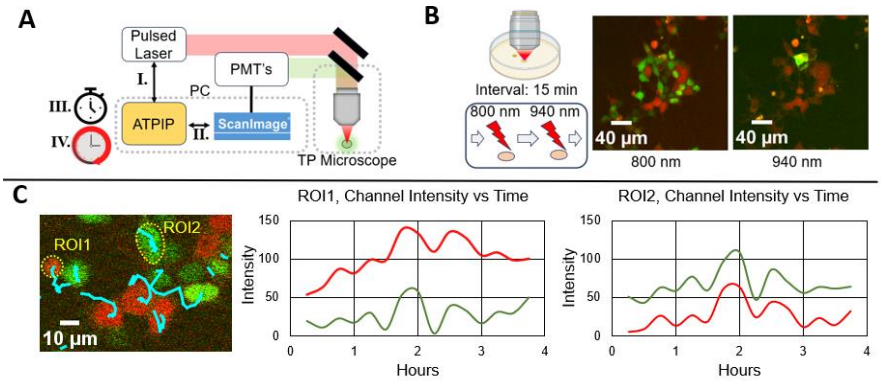

Figure 1. (**A**) ATPIP communicates with laser (**I**) and ScanImage (**II**), manages timing and scheduling of commands (**III**), and generates a timelapse for functional imaging (**IV**). (**B**) Experimental design for imaging HEK293 cells using ATPIP and first scans under 800 nm and 940 nm. (**C**) Cellpose segmentation and TrackMate analysis reveals traces of cells (in blue) with intensity plots for red and green channels of two cells.

Conclusions. ATPIP is a functioning automatic scanning program that allows for spectral and timelapse imaging of live cells, justifying further tests of extended time periods for cell cultures or intravital cell tracking in animals.

[1] Liang, Y., & Walczak, P. (2021). Long term intravital single cell tracking under multiphoton microscopy. *Journal of Neuroscience Methods*, *349*, 109042. https://doi.org/10.1016/j.jneumeth.2020.109042

[2] Stringer, C., Wang, T., Michaelos, M., & Pachitariu, M. (2021). Cellpose: A generalist algorithm for cellular segmentation. *Nature Methods*, *18*(1), 100–106. https://doi.org/10.1038/s41592-020-01018-x

[3] Ershov, D., Phan, M.-S., Pylvänäinen, J. W., Rigaud, S. U., Le Blanc, L., Charles-Orszag, A., Conway, J. R. W., Laine, R. F., Roy, N. H., Bonazzi, D., Duménil, G., Jacquemet, G., & Tinevez, J.-Y. (2022). TrackMate 7: Integrating state-of-the-art segmentation algorithms into tracking pipelines. *Nature Methods*, *19*(7), 829–832. https://doi.org/10.1038/s41592-022-01507-1

Title: Minimally Invasive Brain Tumor Ablation Using PET/CT Model

Authors: Sankar Muthukumar [1], James Crowley [2], Jordan Darden [3], Jackson Kiser [2], Jason Mace [2], Mark Witcher [3]

1 **Virginia Tech Carilion School of Medicine, Roanoke, VA; 2 Department of Radiology, Carilion Clinic, Roanoke, VA; 3 Department of Neurosurgery, Carilion Clinic, Roanoke, VA**

Background: Gliomas represent the most commonly occurring tumors in the central nervous system, accounting for approximately 80% of all malignant primary brain tumors [1]. The current standard of imaging of gliomas involves contrast-enhanced magnetic resonance imaging (CE-MRI), which delineates tumors by identifying sites of blood-brain barrier (BBB) disruption and vascular leakage caused by the tumor. However, this imaging modality faces several limitations, notably its inability to distinguish between tumor pseudoprogression and treatment-related changes, complicating recurrent glioma diagnosis [3]. To address some of the limitations of CE-MRI, positron emission tomography (PET) is increasingly used in clinical practice to image gliomas, demonstrating efficacy in delineating tumor volume and diagnosing recurrent gliomas [4]. However, the use of PET/CT to guide therapies, such as minimally invasive tumor ablation, has not been well explored.

Objectives: Assess if PET/CT can be used to guide minimally invasive brain tumor ablation.

Methods: IRB approved protocol and process to utilize radioactive material.

Biopsy: To simulate areas of radioactive uptake in the brain, we utilized a non-human model - implanting a radioactive fluorine pill inside a watermelon. The model was first imaged using CT and then PET on the Siemens Biograph Vision ^{TM} PET/CT scanner, providing us with baseline scans and coordinates through which we could access the pill using a CT-guided biopsy needle. We then measured the depth needed to access the radioactive pill and inserted the biopsy needle to that distance. Repeat PET/CT imaging was obtained, which showed the needle at the site of radioactivity within the model. Ablation: A similar model was used to assess whether thermal ablation could target the site of radiation and whether it could be assessed on PET/CT imaging. After obtaining preliminary PET/CT scans and assessing the depth to the radioactive pill, we introduced a catheter to reach the location of the pill for thermal ablation. We then ablated the site twice, the first for 1 minute at 9W then for 2 minutes at 15W.

Results: In successfully localizing the area of radioactivity within the PET/CT brain model, we were able to determine that this imaging modality was practical. However, we faced challenges with the implementation of the procedures guided by PET/CT. In our biopsy model, while we were able to localize the radioactive pill on a 2D plane and determine the necessary depth, we faced problems with the angle of entry of the biopsy needle and guiding the needle through a 3D space. In the thermal ablation portion, our laser did not make any discernible effect on the area of radiation, likely due to the composition of the watermelon.

Conclusions: While PET/CT imaging may be an effective imaging modality for guiding minimally invasive procedures in the brain, our model was unsuccessful in evaluating for post-ablative changes. We are currently working to refine our model to a protein-based material which works better with our thermal ablation capabilities. We intend to repeat this experiment after a more effective model and protocol is established.

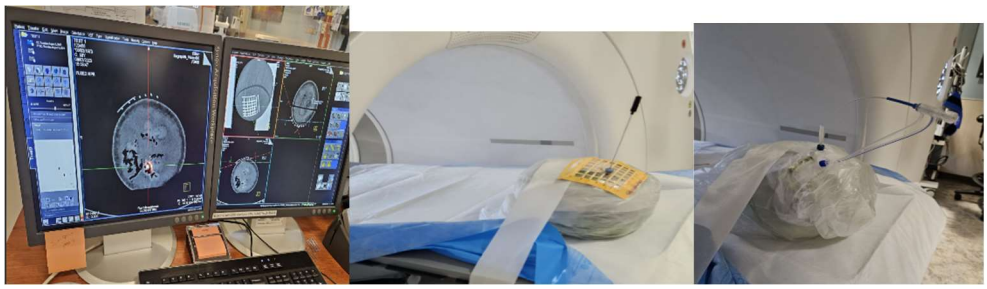

References:

1. Hanif F, Muzaffar K, Perveen K, Malhi SM, Simjee Sh U. Glioblastoma Multiforme: A Review of its Epidemiology and Pathogenesis through Clinical Presentation and Treatment. *Asian Pac J Cancer Prev*. Jan 1 2017;18(1):3-9. doi:10.22034/APJCP.2017.18.1.3

2. Hu LS, Hawkins-Daarud A, Wang L, Li J, Swanson KR. Imaging of intratumoral heterogeneity in high-grade glioma. *Cancer Lett*. May 1 2020;477:97-106. doi:10.1016/j.canlet.2020.02.025

3. Brandsma D, van den Bent MJ. Pseudoprogression and pseudoresponse in the treatment of gliomas. *Curr Opin Neurol*. Dec 2009;22(6):633-8. doi:10.1097/WCO.0b013e328332363e

4. Nihashi T, Dahabreh IJ, Terasawa T. Diagnostic accuracy of PET for recurrent glioma diagnosis: a meta-analysis. *AJNR Am J Neuroradiol*. May 2013;34(5):944-50, S1-11. doi:10.3174/ajnr.A3324

Precise Induction of Autoimmune Demyelinating Lesions in Rat Brain Using Focused Ultrasound: A Robust Model for Multiple Sclerosis

Lukasz Kalkowski, PhD[1]; Guanda Qiao, MD, PhD[1]; Pavlos Anastasiadis, PhD[2]; Yajie Liang, PhD; Piotr Walczak, MD, PhD[1]
1 Department of Diagnostic Radiology and Nuclear Medicine, University of Maryland School of Medicine, Baltimore, MD, USA
2 Department of Neurosurgery, University of Maryland School of Medicine, Baltimore, MD, USA

Background: In the pursuit of addressing the need for the efficacious treatment for multiple sclerosis (MS), a promising avenue is cell therapy. This approach entails the transplantation of myelin-producing cell populations, offering a potential path to recovery from the debilitating effects of demyelination. However, this strategy faces challenges, difficulties including suboptimal cell delivery, harnessing their full therapeutic potential, and improving fidelity of disease models.
Objective: Our overarching aim is to establish a robust platform for glial-restricted progenitors (GRPs) based cell therapy. To facilitate reliable efficacy studies, we are currently developing a model of localized autoimmune demyelination in the rat's brain. Such a model with spatially controlled lesion placement will help understand autoimmune pathomechanism of MS and interpret outcomes of MRI-guided intraarterial delivery of GRPs.
Methods: Lewis rats were immunized with anti MOG_{1-125} solution in incomplete Fruend's adjuvant and after two weeks proceeded for tabletop focused ultrasound BBBO (**Fig. 1A**). The animals' anti-MOG_{1-125} IgG were analyzed using ELISA and the BBB status, as well anatomical changes were assessed by post-FUS MRI. Follow-up MRI was performed 8-10 days post-FUS. Animals were then euthanized and perfused, and the brain samples were analyzed by histopathology.
Results: Blood anti-MOG IgG levels were assessed 2 weeks after immunization; out of 9 experimental animals, low level autoimmunity was detected only in three rats. MRI (**Fig. 1B-F**) indicates BBB opening, however, noticeable hemorrhage was observed in the brain tissue. No neurological impairment was found during the experiment.
Conclusions: The preliminary findings underscore the feasibility of inducing autoimmunity while also precisely situating brain lesions through the utilization of focused ultrasound-mediated blood brain barrier opening. Nevertheless, it is evident that further enhancements are imperative for this model.

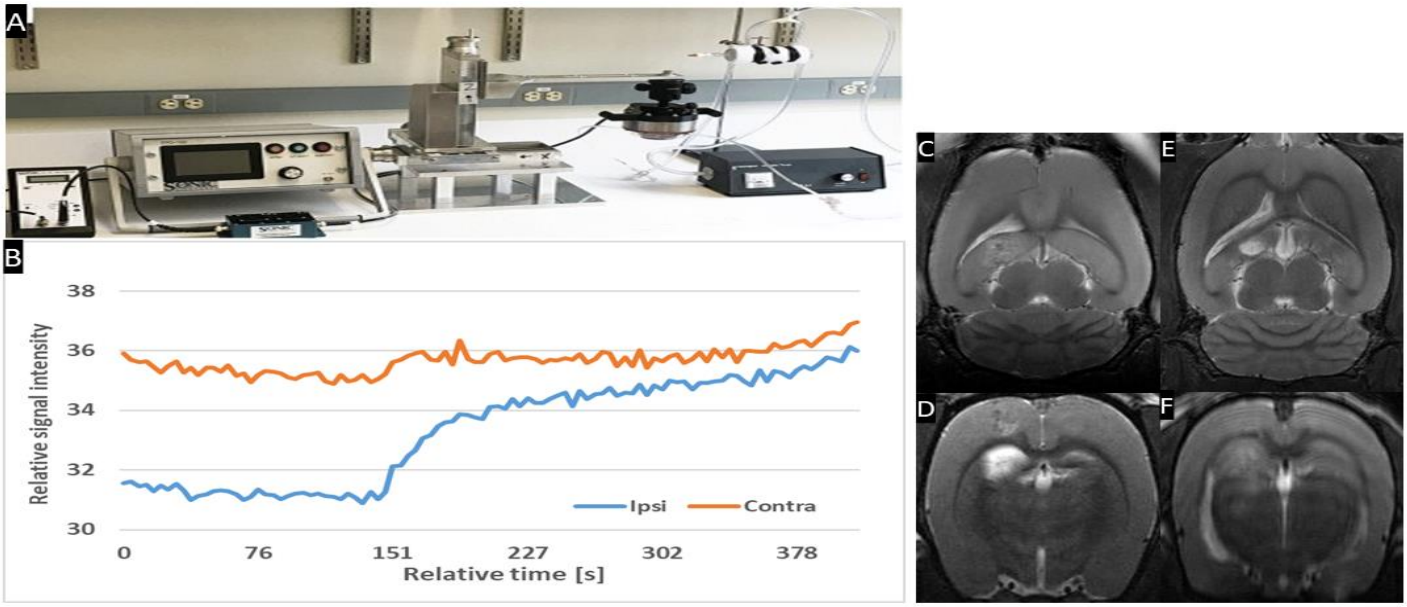

Fig. 1. Overview of the FUS system, based on Biomed Eng Online. 2019; 18: 36 (A); the contrast enhancement dynamics acquired from DCE MRI at sonication ("ipsi") area and corresponding contralateral area; T2-weighted images taken after the sonication (C,D) as well as 9 days post-FUS (E,F).

Non-Invasive Evaluation of Mouse Kidney Function Through Imidazole MR-CEST Urography: Insights into pharmacokinetics

Zinia Mohanta[1] PhD, Julia Stabinska[1] PhD, Aruna Singh[1] PhD, Martin Pomper[1] MD, PhD, Farzad Sedaghat[1] MD, Max Kates[2,3] MD, Michael T. McMahon[1,4] PhD

AFFILIATIONS: Department of [1]Radiology, [2]Urology, [3]Oncology, Johns Hopkins University, School of Medicine; [4]F. M. Kirby Research Center for Functional Brain Imaging, Kennedy Krieger Institute, Baltimore, MD, United States

Background: Chemical exchange saturation transfer magnetic resonance imaging (CEST MRI) is an advanced imaging technique in which compounds containing exchangeable protons are selectively saturated within a biological tissue and then this saturation is gradually transferred to water molecules thus facilitating enhanced contrast for sensitive MR imaging[i]. Chemical contrast agents also have been designed to non-invasively report diagnostic physicochemical properties of the tissue in which such agents distribute (e.g. pH of kidneys)[ii]. CEST MRI pH mapping has emerged as a promising approach to assess the acid-base homeostasis in the kidney and for monitoring pH changes in several disease models that affect renal pH. Imidazole-4,5-dicarboxamide-diglutamate (I45DC-diGlu) is a new anionic small molecule CEST MRI pH imaging contrast agent that has a large labile proton chemical shift (7.7 ppm from water) due to intramolecular hydrogen bonding and a second labile proton at 4.5 ppm[iii]. These protons have very different exchange dependence on pH, which allows ratiometric, concentration-independent pH measurements. This I45DC scaffold offers greater synthetic flexibility to adjust the proton exchange properties and biodistribution[iv].

Objective: Systematic evaluation of pharmacokinetics, biodistribution, and organ toxicity of Imidazole-4,5-dicarboxamide-diglutamate (I45DC-diGlu). Demonstrate greater synthetic flexibility to adjust the proton exchange properties and biodistribution for a specific biomedical application in comparison to existing agents.

Methods: C57BL/6J mice were administered increasing doses of I45DC-diGlu (125 - 1,000 mg/kg) through a tail vein injection and then an imaging protocol was optimized for pH mapping of the kidneys using a 11.7 T MRI scanner. Saturated CEST images were captured at 4.5 and 7.7 ppm over a course of ~30 minutes after injection. A pH calibration curve was obtained from I45DC-diGlu phantoms of different pH values. Renal pH values were calculated using the signal ratio for 4.5 and 7.7 ppm against the pH calibration curve. Contrast-time activity curves and pH maps were obtained using saturation pulses with T_{sat} = 2 sec and B_1 = 5.0 mT, using a single shot rapid acquisition with relaxation enhancement sequence and centric encoding. We also characterized pharmacokinetic properties of this agent.

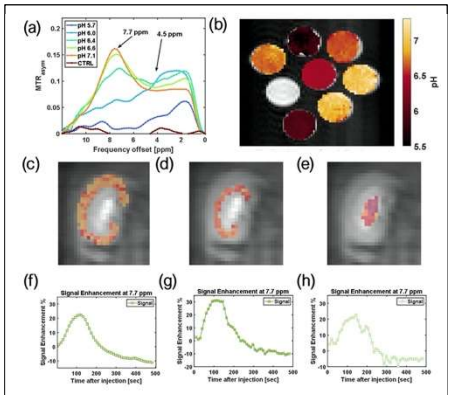

(a) ROI based MTR_{asym} spectra and (b) in vitro pH maps of I45DC-diGlu phantoms at different pH values at saturation power of 5 μT (c,d,e) in vivo pH maps and (f,g,h) contrast-time activity curves generated for the corresponding ROIs

Results: CEST MRI time-activity curves indicated rapid renal excretion with $t_{½}$ ~160 sec. We confirmed accuracy of our analyses by measuring the average pH for the whole kidney tissue at peak contrast and found our values matched reported values (pH ~ 6.8). We then performed compartmentalized analyses of the cortex, outer-, and inner-medullary regions and measured pH distribution and time-dependent contrast activity across these regions of interest (ROI). We calculated the pH to be 6.84 ± 0.11, 6.73 ± 0.14 and 6.55 ±0.05 and observed CEST contrast of 24%, 30% and 22%, respectively.

Conclusion: Herein, we have identified a sensitive probe to accurately measure tissue pH within different regions of the kidney. Our process paves the path for further preclinical investigation and assessment of this probe in higher species and presents a new scaffold to develop new pH mapping CEST agents.

References:

[i] van Zijl PC, Yadav NN. Magn Reson Med. **2011**;65(4):927-48.

[ii] Longo DL, Sun PZ, Consolino L, Michelotti FC, Uggeri F, Aime S. J Am Chem Soc. **2014**;136(41):14333-14336.

[iii] Bo S, Sedaghat F, Pavuluri K, Rowe SP, Cohen A, Kates M, McMahon MT. Tomography. **2021**;7(1):80-94.

[iv] Yang X, Song X, Ray Banerjee S, Li Y, Byun Y, Liu G, Bhujwalla ZM, Pomper MG, McMahon MT. Contrast Media Mol Imaging. **2016**;11(4):304-12.

Exploring the potential of MRI CEST pH imaging as a hypoxia marker: Distinguish between hypoxic and non-hypoxic tumors

Aruna Singh[1,2], Julia Stabinska[1,2], Balaji Krishnamachary[2], Farzad Sedaghat[3], Sridhar Nimmagadda[2], Jeff Bulte[2], Zaver Bhujwala[2], Michael T Mcmahon[1,2]

[1]Russell H. Morgan Department of Radiology and Radiological Science, Johns Hopkins University School of Medicine, Baltimore, MD, United States, [2]F.M. Kirby Research Center for Functional Brain Imaging, Kennedy Krieger Institute, Baltimore, MD, United States, [3]James Buchanan Brady Urological Institute and Department of Urology, Johns Hopkins University School of Medicine, Baltimore, MD, United States

Keywords: chemical exchange saturation transfer (CEST), hypoxia, acidosis, pH, iopamidol, MDA-MB 231, Hypoxia inducible factor-1 alpha (HIF-1alpha)

Background: Acidosis and hypoxia are two features of the tumor microenvironment that result in immune evasion, aggressiveness and resistance to therapy. Tumor acidity is generally considered to be a result of the metabolic shift caused due to stabilization of hypoxia inducible factors (HIFs) and further transcriptional activation of target genes by HIFs leading to accumulation of extracellular lactic acid.[1,2] Acidosis is emerging as a marker for cancer proliferation, metastasis, aggressiveness and resistance. In this study, using genetically engineered MDA-MB-231 breast cancer cells to stably downregulate HIF-1α (231- HIF-1α shRNA), we investigated CEST MRI based pH mapping as a tool to detect changes in HIF expression in a xenograft mouse model.

Objectives: To use MR CEST pH imaging for studying hypoxia in solid tumors

Methodology: Two groups of murine breast tumor models were used for the study by inoculating ~2 million 231-HIF-1α shRNA or an empty vector expressing (231-EV) MDA-MB-231 cell line in the mammary fat pad of female SCID mice. These cells lines have been characterized previously for HIF expression. MR pH imaging was conducted on an 11.7 T Bruker horizontal bore animal scanner using an eight-channel mouse body phased-array receive coil. Z-spectra were acquired using a single-shot RARE sequence with centric encoding, parameters: TR/TE=6.5s/3.5 ms preceded by a ω =3.6 μT T =4 s saturation pulse and a fat-suppression module, acquisition matrix =64x64 reconstructed to 128x128, FOV =3x3cm, slice thickness=1.5mm. A series of 61 MR frequencies were acquired in the frequency offset range ±10 ppm. MR CEST images were repeated eight times, once before and seven times after intravenous injection of Iopamidol contrast agent (dose = 4 g iodine/kg bw). For pH mapping, post-injection magnetization transfer ratio (MTR) values at 4.3 and 5.5 ppm were quantified at 30 min post-injection. Pre-injection MTR maps were then subtracted from the post-injection MTR images to remove endogenous CEST signals. Tumor pH values were obtained by calculating the concentration-independent saturation transfer ratio $R_{ST}=(1-MTR_{4.3ppm})\times MTR_{5.5ppm}/((1-MTR_{4.3ppm})\times MTR_{5.5ppm})$ and using a pH calibration with MTR values of 25 mM Iopamidol in PBS followed by titration to pH values of 5.8, 6.1, 6.4, 6.7, 7.0 and 7.3.

Results: Western blots of 231-EV and 231-HIF-1α shRNA cells exposed to 4 hours of true hypoxia confirmed absence of hypoxia induced HIF-1α expression in knockdown cells. Figure 1a shows the pH dependence of two amide protons of Iopamidol resonating at 4.3 and 5.5 ppm. As observed from MTR vs. pH plots, the CEST effect is markedly pH-dependent for both pools of exchangeable protons, Figures 1b-g shows T2-weighted anatomical images (b, d), CEST pH maps overlaid over anatomical images (c, e) and pH histograms (f, g) for the two types of tumors. Both breast cancer models showed a marked extracellular acidification with average extracellular pH (pHe) values of 6.1 and 6.2 for MDA-MB-231 and MDA-MB-231 HIF-1α shRNA tumors, respectively with n=3 mice per group.

Conclusion: Our preliminary study shows that CEST MRI-based pH imaging of tumors may be a valuable tool for predicting the hypoxic nature and identifying tumors with aggressive phenotype.

References: 1. Corbet C, Feron O. *Nat Rev Cancer*. 2017 Oct;17(10):577-593.
2. B Philip, K Ito, R Moreno-Sanchez, SJ Ralph. *Carcinogenesis*, 34 (2013), pp. 1699-1707.

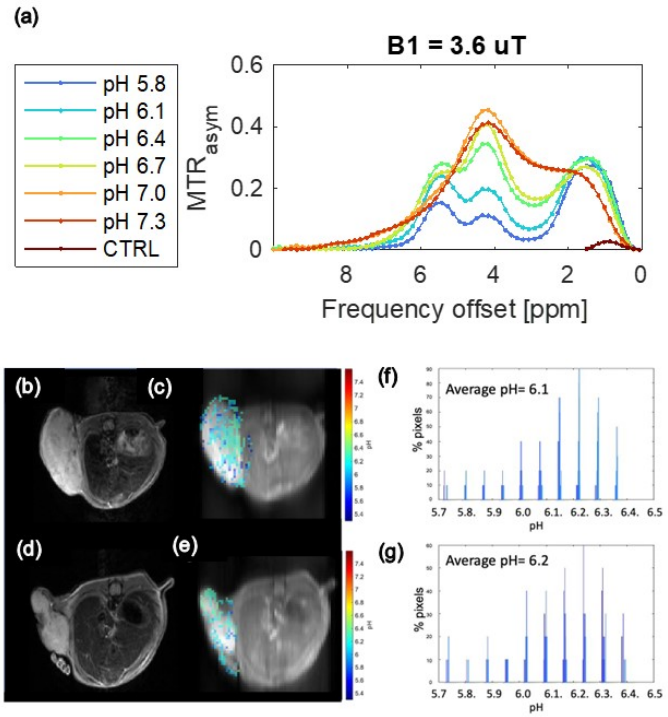

Figure 1: (a) MTRasym vs pH plot for two sets of amide protons of iopamidol resonating at 4.3 and 5.5 ppm at saturation frequency of 3.6μT T2 weighted images;

(b-g) CEST pH maps and pH histograms of two groups of tumour models. (b) and (d) - T2 weighted images of MDA-MB 231 and MDA-MB 231 HIF-1 alpha shRNA tumours respectively;

(c) and (e) - CEST pH maps of MDA-MB 231 and MDA-MB 231 HIF-1 alpha shRNA tumours respectively;

(f) and (g) - pH histograms from MDA-MB 231 and MDA-MB 231 HIF-1 alpha shRNA tumours respectively.

Optical Imaging-Guided Cell Transplantation for Improved Cell Loading Efficacy

Jinghui Wang, Colleen Russell, Mikolaj Walczak, Miroslaw Janowski, Piotr Walczak and Yajie Liang
Department of Diagnostic Radiology and Nuclear Medicine, University of Maryland School of Medicine, Baltimore, MD. Corresponding author: Yajie.liang@som.umaryland.edu

Background

Optical imaging-guided transplantation of mouse cerebral cortex cells combines the advantages of optical imaging and precise neurointerventions. In neuroscience research, optimizing delivery procedures in the mouse cerebral cortex is critical for the accurate and efficient manipulation of neural circuits.

Objective

We hypothesized that using the pulse-elevation mode of cell delivery can significantly improve cell loading efficiency in the needle track of the mouse brain.

Methods

Mouse neural stem cells (C17.2 cells) stably expressing the fluorescent protein Venus through transduction with lentiviral vector FCIV were injected at the concentration of 2.5×10^6 cells/ml to 0.6 % low-melting agarose [1] or the mouse brain at the coordinates: AP -3.35 mm, ML 1.75 mm using the stereotaxic instrument. The target depth for cell transplantation was set at 500 μm. Before injection, the needle was extended to 700 μm and then withdrawn to a target depth of 500 μm. Infusion program settings: step1: rate: 0.1 μL/min, 20 nL; delay 20 s and withdraw to 0.4 μm; step2: rate: 0.1 μL /min, 20 nL; delay 20 s and withdraw needle to 0.3 μm; step3: rate: 0.1 μL /min, 20 nL; delay 20 s and withdraw needle to 0.2 μm. Leica DMi8 was used to capture fluorescent images *in vitro*. For the *in vivo* experiment, 2-photon imaging was applied on days 0, 1, and 2 [2].

Results

In the *in vitro* experiment, we found a significant difference between the pulse-elevation and pulse groups. The cell signal in the pulse-elevation group needle track was significantly higher than in the pulsed group (**Figure 1a**). *In vivo*, using the same infusion procedure, we observed a clear needle track post-surgery on day 0, and cells were confined to the needle track (**Figure 1c**). On day 1 and day 2, we imaged the same brain area but found scattered cells around the injected area, implying active migration of C17.2 cells out of the injection site (**Figure 1d** and **1e**). These observations suggest that the pulsed-elevation injection can precisely deliver and hold cells within the needle track and improve loading efficiency to the mouse brain.

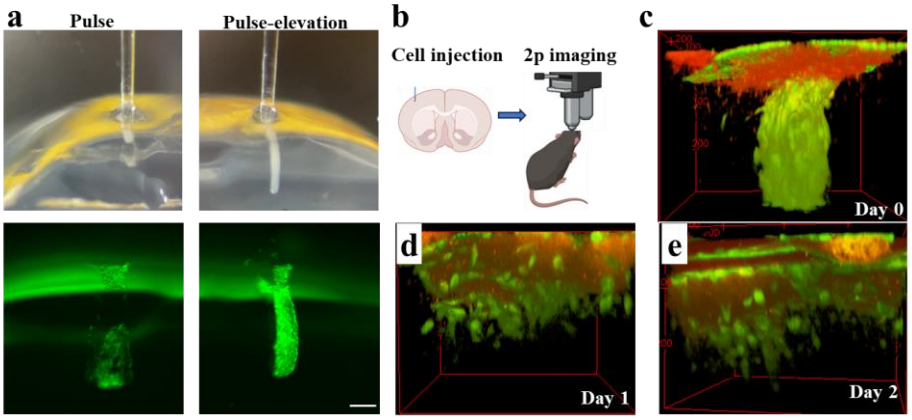

Figure 1 (**a**) Design of in vitro experiments and images of needle tracks under a Leica microscope; (**b**) Design of in vivo experiment; (**c-e**) 3D view of the imaging stack showing transplanted cells in needle track on day 0 (**c**), 1 (**d**), and 2 (**e**). Scale bar in (**a**), 100 μm

Conclusions

We established a platform for optical imaging-guided cell transplantation into the mouse cerebral cortex. Through *in vitro* and *in vivo* experiments, we found that the pulse-elevation injection method significantly increases cell transplantation's efficacy and improves cell loading efficiency. Further evaluation of this preliminary findings is warranted.

Reference

1. Chen ZJ, Gillies GT, Broaddus WC, Prabhu SS, Fillmore H, Mitchell RM, Corwin FD, Fatouros PP. *A realistic brain tissue phantom for intraparenchymal infusion studies.* J Neurosurg. 2004 Aug;101(2):314-22. doi: 10.3171/jns.2004.101.2.0314. PMID: 15309925.
2. Liang Y, Walczak P. *Long term intravital single cell tracking under multiphoton microscopy.* J Neurosci Methods. 2021 Feb 1;349:109042. doi: 10.1016/j.jneumeth.2020.109042. Epub 2020 Dec 16. PMID: 33340557.

Downfield 3D proton MRSI of the human brain: initial results at 7T

İpek Özdemir[1] and Peter B. Barker[1,2]

[1]Russell H. Morgan Department of Radiology and Radiological Science, The Johns Hopkins University School of Medicine, [2]F.M. Kirby Center for Functional Brain MRI, The Kennedy Krieger Institute, Baltimore, MD

Background

We have previously implemented 3-dimensional (3D) proton magnetic resonance spectroscopic imaging (MRSI) of resonances downfield (DF) from water in the human brain at the widely available field strength of 3 Tesla (T)[1]. In this abstract, initial results are presented for 3D DF-MRSI at 7T. DF-MRSI at 7T is hypothesized to show improved signal-to-noise ratios (SNR) and spectral resolution compared to lower field strengths, but also to exhibit more variability due to increased B_0 and transmit B_1 field inhomogeneity.

Objective

To implement 3D DF-MRSI in the human brain at 7T with whole brain coverage.

Methods

All scans were performed on a Philips 7T 'Achieva' scanner equipped with an 8-channel transmit/32-channel receive head coil (Nova Medical). 3D DF-MRSI was implemented as described previously at 3T[1], with $1\bar{3}3\bar{1}$ spectral-spatial excitation and frequency selective refocusing. Because of the greater chemical shift dispersion at 7T, the $1\bar{3}3\bar{1}$ inter-pulse delay was shortened from 1.45 to 0.70 msec, and the bandwidth of the selective refocusing pulse increased from 400 to 900 Hz, which allows TE to be shortened to 15 ms compared to 22ms at 3T. Other scan parameters were 1 transient, flip angle 64˚, circular phase-encoding, FOV 200x180x120 mm, 120 mm excitation slab thickness, TR 282 ms, matrix size 29x26x8, giving a nominal spatial resolution of ≈7x7x15 mm = 0.7 cm^3 and a scan time of 22m:16s. 2nd order shimming was performed prior to MRSI.

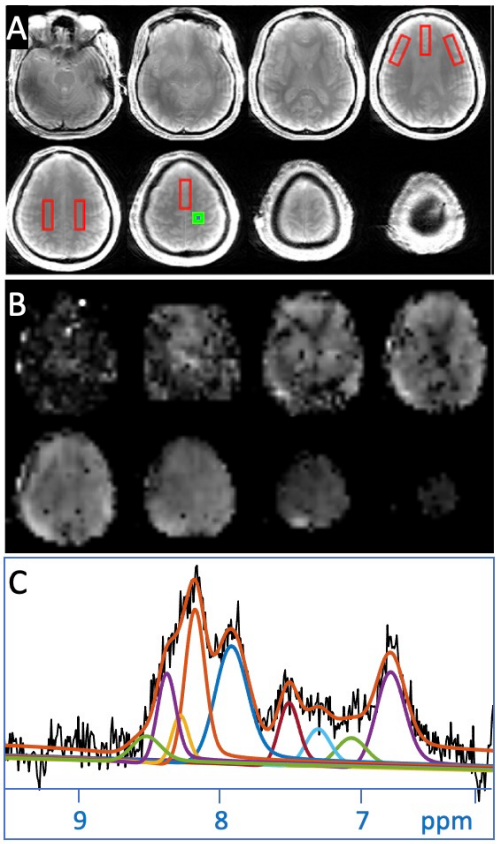

DF-MRSI data were analyzed using 'LCModel' fitting with a basis set consisting of 9 Gaussian peaks ranging in frequency from 6.83 to 8.49 ppm as described previously[1]. Frequency correction was performed based on the H_20-MRSI, and residual water removed using an HLSVD filter. The peaks in the amide region of the spectra (8.1 to 8.4 ppm) were summed together ('8.x'). SNR was measured in selected regions (Fig. 1A) from the height of the 8.18 ppm peak divided by the standard deviation of the noise in the -1 to -2 ppm region.

The protocol was tested in a normal volunteer (M, 58 yrs). In addition to 3D DF-MRSI, an unsuppressed water MRSI was also recorded with the same voxel size and geometry as the DF sequence, as well as proton density (PD) localizer images, and a 3D T_1w MPRAGE scan. Total scan time was approximately 45 minutes.

Results

Fig. 1A shows PD localizer images of the 8 slices covered by MRSI and regions of interest used for analysis (in red), and 1B shows reconstructed '8.x' amide images. Figure 1C shows an example spectrum and LCModel analysis from left posterior frontal lobe gray matter (slice 6, voxel location indicated in green on 1A). Average SNR values were 20.5 in anterior cingulate, 24.2 in centrum semiovale, and 23.4 in dorsolateral prefrontal cortex.

Conclusions

3D DF-MRSI of human brain at 7T is feasible, but more work is required to improve spatial uniformity of reconstructed metabolic images, and to perform a systematic comparison to DF-MRSI data recorded at 3T.

References

1. Özdemir, İ, Ganji, S, Gillen, J, Etyemez, S, Považan, M, Barker, PB. Downfield proton MRSI with whole-brain coverage at 3T. Magn Reson Med. 2023; 90(3): 814- 822.

Reduced Brain Entropy in Depression by Two Types of Interventions

Alishba Sadiq[1], Gianpaolo Del Mauro[1], Ze Wang[1]
[1]Department of Diagnostic Radiology & Nuclear Medicine, University of Maryland School of Medicine, Baltimore, MD, United States

Background:

Resting-state fMRI (rsfMRI)-derived brain entropy (BEN) has been shown to be related to biological, neuro-pathological, and behavior measures and sensitive to neuromodulation and medication [1]. Increased BEN was reported in depressive patients [2], but it remains unclear how BEN responds to different interventions. The purpose of this study was to assess BEN changes in major depression patients who underwent either of two types of intervention: electroconvulsive therapy (ECT) and sleep deprivation therapy (TSD).

Methods:

All data were collected at the University of California, Los Angeles. 53 depression patients underwent TSD. 23 depressed patients underwent ECT. BEN maps were calculated from rsfMRI data before and after interventions using BENtbx [3]. Paired-t test was used to assess the effects of interventions on BEN. Statistical significance was defined by voxel-wise $p < .001$ and a cluster-wise $p < .05$ (multiple comparison corrected using the family-wise error method).

Results:

Reduced BEN was observed after both interventions. ECT reduced BEN in precuneus/posterior cingulate cortex (PCu/PCC), and bilateral parietal cortex. TSD reduced BEN in PCu/PCC, superior temporal cortex, motor and visual cortex. Furthermore, the assessment of depressive symptoms using the Hamilton Depression Rating Scale (HDRS) has revealed noteworthy findings. Specifically, there is an observable reduction in the total score after both TSD and ECT treatments (Figure 1). This reduction indicates a decrease in the severity of depressive symptoms, suggesting a beneficial effect of treatments.

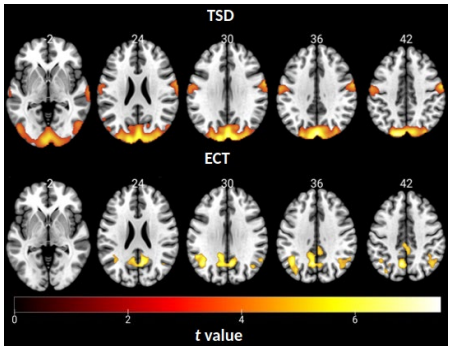

Figure 1: Brain entropy (BEN) changes within specific brain regions resulting from total sleep deprivation (TSD) and electroconvulsive therapy (ECT) interventions.

Discussion and conclusions:

We reported that two independent interventions can both suppress BEN in depression especially in parietal cortex. Since depression was found to be associated with increased BEN, our results indicate a success of the interventions and suggest that effects of interventions may be through modulating brain activity irregularity or coherence as reflected by BEN.

1. Zhou F, Zhuang Y, Gong H, et al. (2016) Resting State Brain Entropy Alterations in Relapsing Remitting Multiple Sclerosis. PLOS ONE 11(1): e0146080. https://doi.org/10.1371/journal.pone.0146080

2. Roy AV, Thai M, Klimes-Dougan B, et al. (2021). Brain entropy and neurotrophic molecular markers accompanying clinical improvement after ketamine: Preliminary evidence in adolescents with treatment-resistant depression. J Psychopharmacol. 2021 Feb;35(2):168-177. https://doi.org/10.1177/0269881120928203

3. Wang Z, Li Y, Childress AR, Detre JA (2014) Brain Entropy Mapping Using fMRI. PLOS ONE 9(3): e89948. https://doi.org/10.1371/journal.pone.0089948

Spatial Heterogeneity of Renal Function: Novel Application of New Geometry SPECT/CT

Jason Chen, Aaron Sheppard, Roberto Maass-Moreno, Michael Collins, and Babak Saboury

Radiology and Imaging Sciences, Clinical Center, National Institute of Health, Bethesda, MD

Background: Traditional ^{99m}Tc-MAG3 planar renal scan is limited by its two dimensional nature of the scan, low resolution, limited contrast, and a lack of a CT for anatomical context. It can only provide total kidney function without showing the kidney's regional or segmental functional differences. A renogram obtained via a full ring SPECT/CT however, provides three dimensional information of the kidneys. Based on the CT segmentation, it is then possible to define corresponding regional renal function.

Objective: To map regional/segmental renal function based on ^{99m}Tc-MAG3 SPECT/CT renal scan

Methods: On the transaxial view of the CT scans, contours of the kidneys were drawn slide by slide (2.5 mm) from top to bottom, including renal cortex alone, renal pelvis alone, and whole kidney separately, based on the visual density. These slides were then displayed in the coronal view fused with the corresponding SPECT renal scan. Mean and Total counts of each contour over each SPECT slide were determined by the MIM software automatically. Activity versus time curves were then generated. As an example to measure regional renal function, in this study, the whole kidney is arbitrarily divided into three parts and the corresponding regional function is determined to demonstrate feasibility of this methodology.

Results: A ^{99m}Tc-MAG3 SPECT/CT renal scan was obtained from a patient with a normal right kidney and a hydronephrotic left kidney. As an example to measure the regional/segmental function of the kidney, we divided both kidneys into thirds based on CT: top, middle, and bottom thirds. As expected, the functions of each ⅓ are different from one another, with the middle ⅓ showing the highest function in the normal kidney (Figures 1c and 1d), while the hydronephrotic left kidney did not show substantial differentiated regional function (Figures 1e and 1f), likely due to retention of counts ipso facto of the kidneys hydronephrosis. Similar results can be seen when the kidneys are segmented based on just the renal cortex alone (Figure 2), not the whole kidney (Figure 1). This means that in real practice, regional renal function can be mapped.

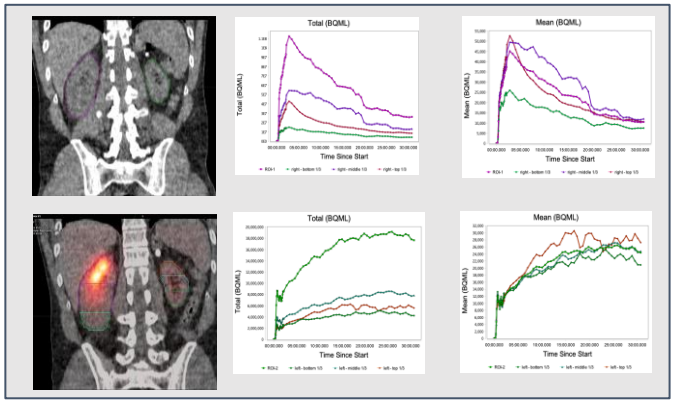

Figure 1

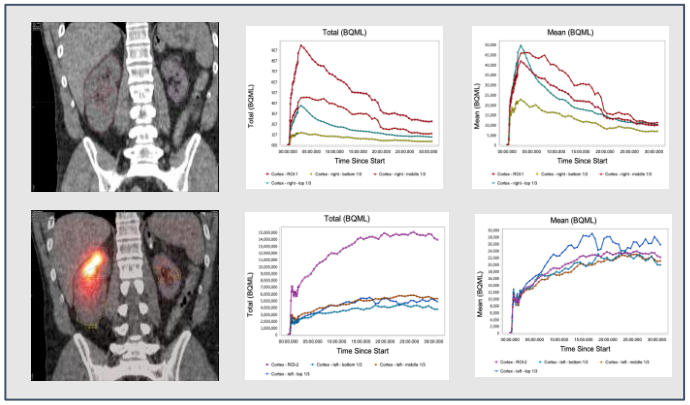

Figure 2

The kidneys were segmented into 3 parts equally based on the whole kidney (Figure 1) and cortex alone (Figure 2) in a patient with a normal right kidney and a hydronephrotic left kidney. a. Segmentation of the kidneys on CT (a) which was fused to SPECT (b). Time activity curve of the 3 divisions of the kidneys and the whole kidney was determined by the MIM software based on the total counts (c: right kidney, e: left kidney), and mean counts (d: right kidney, f: left kidney)

Conclusion: Our results show that, different from planar ^{99m}Tc-MAG3 renal scan, ^{99m}Tc-MAG3 SPECT/CT can obtain regional/segmental renal function. The methodology provides an additional tool for estimation of regional renal function in patients with conditions such as renal tumors, scarring, or other diseases.